Friedrich-Alexander-Universität
Erlangen-Nürnberg

Department für Physik
Lehrstuhl für Physik

D I P L O M A R B E I T

Spatially Resolved X-Ray Analysis and Modeling of the Non-Thermal Emission of the Pulsar Wind Nebula G0.9+0.1

Markus Holler

15. Oktober 2010

Gutachter:
1. Prof. Dr. Ch. Stegmann
2. Prof. Dr. J. Wilms

Kurzfassung

In der vorliegenden Diplomarbeit wird die nichtthermische Strahlung des Pulsarwindnebels im Supernovaüberrest G0.9+0.1 umfassend untersucht. Mit Hilfe von Daten des *XMM-Newton*-Satelliten werden die spektralen Eigenschaften von Röntgenphotonen aus ringförmigen Regionen analysiert, welche auf die Position des Pulsars von G0.9+0.1 zentriert sind. Im Anschluss daran wird ein radialsymmetrisches, leptonisches Modell angewendet, um die gemessene Röntgenemission zu reproduzieren und die Eigenschaften des Pulsarwindes zu verstehen. Durch die mit den optimierten Modellparametern berechnete Synchrotronstrahlung können die spektralen Eigenschaften der gewählten Regionen gut nachvollzogen werden. Unter der Annahme, dass die selbe Leptonpopulation Photonen durch den inversen Comptoneffekt in den Hochenergiebereich streut, wird diese Strahlung mit dem gleichen Modell unter der Verwendung der zuvor optimierten Parameter berechnet. Die Ergebnisse werden anschließend mit den veröffentlichten Daten von H. E. S. S. verglichen. Es zeigt sich, dass sowohl die spektrale Form als auch der Photonfluss abweichen. Dies wird allerdings bis zu einem gewissen Grad erwartet, da die Modellierung nur einen kleinen Teil des Pulsarwindnebels betrachtet. Im Gegensatz dazu entsprechen die H. E. S. S.-Daten der kompletten Hochenergiegammastrahlung von G0.9+0.1.

Abstract

The present thesis comprises an extensive study of the non-thermal radiation of the pulsar wind nebula in the supernova remnant G0.9+0.1. Analyzing X-ray data of the *XMM-Newton* satellite, the spectral properties of annulus-shaped regions, centered on the position of the pulsar of G0.9+0.1, are examined. Afterwards a radially symmetric, leptonic model is applied in order to reproduce the measured X-ray emission and understand the properties of the pulsar wind nebula. The synchrotron radiation calculated with the optimized parameters of the model is well able to explain the spectral properties of the chosen extraction regions. Assuming that the same lepton population also scatters photons up to very high energies through inverse Compton scattering, this emission is calculated with the same model using the best-fit parameters of the previous parameter optimization. The obtained results are afterwards compared with the published H. E. S. S. data in the very high energy range. It shows that the spectral shape as well as the photon flux deviate. This is however expected to some degree since the modeling only attempts to reproduce emission from a small part of the pulsar wind nebula. In contrast to that, the H. E. S. S. data corresponds to the overall emission of G0.9+0.1 in very high energy γ-rays.

Contents

1. Introduction

One can only guess how much the cosmic event of the supernova (SN) in the early summer of 1054 AD must have both puzzled and fascinated the people at that time. The guest star with a magnitude of up to $m_{\mathrm{v}} \approx -5$ was visible during daytime for more than 20 days and at the night sky for about two years (Collins et al. 1999). Although there were a few SNe recorded in the medieval times, modern astronomy has a certain relation to that particular one. While the remnants of the other recorded SNe show a shell-type morphology, the one associated with SN1054 is a luminous pulsar wind nebula (PWN) (called the Crab nebula) which radiates all over the observable energy range, from radio wavelengths up to very high energy (VHE) γ-rays with energies above 100 GeV. Fig. 1.1 shows a composite image of the Crab nebula. The different colors correspond to infrared, optical and X-ray data.

Due to the continuous improvement of astronomical instrumentation over the last decades, the number of sources identified as PWNe has been steadily increasing. Their broadband emission is assumed to originate from a leptonic outflow which emits photons through synchrotron radiation and the inverse Compton (IC) effect.

In the course of this thesis, the PWN G0.9+0.1 is studied in detail. After a precise spec-

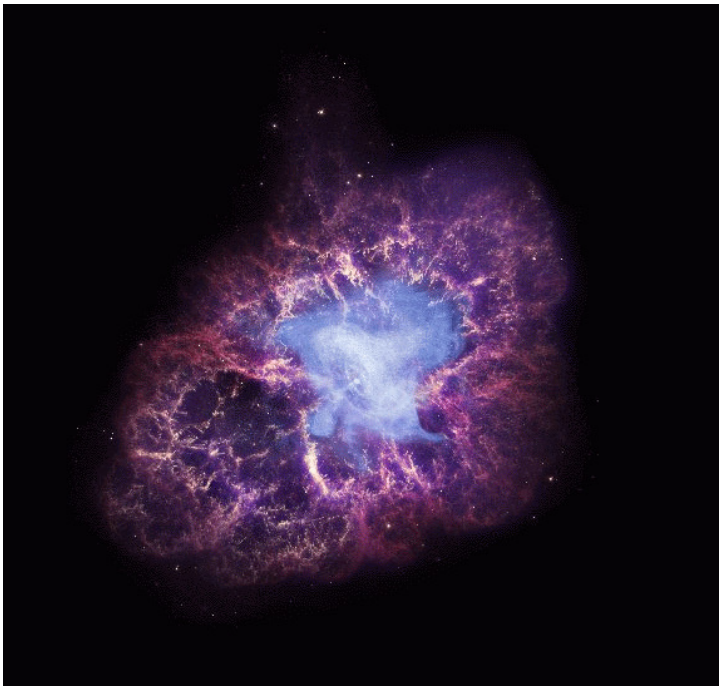

Fig. 1.1.: *Composite image of the Crab nebula. Shown in blue is the X-ray emission observed with Chandra. Yellow and red correspond to optical emission as seen by the HST and purple to infrared measurements from Spitzer. Image taken from Slane (2010).*

tral analysis of several annulus-shaped regions in X-rays, we check the leptonic origin by applying a model which aims to reproduce the observed radiation. The model parameters are optimized by comparing the measured X-ray emission with the modeled synchrotron radiation. Following the presentation of the results, the same model is then used once again with the optimized parameter set in order to calculate the IC emission of the PWN. In the end, the obtained radiation is compared with measured data from H. E. S. S. in the VHE range.

2. The Pulsar Wind Nebula G0.9+0.1

In the first part of this Chapter, the current state of research about PWNe is briefly summarized. The second part comprises a multiwavelength overview of the particular supernova remnant (SNR) and the central PWN discussed in this work, G0.9+0.1. The last part covers the information about PSR J1747−2809, the pulsar powering G0.9+0.1.

2.1. General Properties of Pulsar Wind Nebulae

Not every SNR contains a PWN, as was already mentioned in Chapter 1. In the following, we will give an overview about PWNe and their radiation mechanisms in order to provide a basic understanding of the origin of these objects.

2.1.1. The Pulsar and its Wind

The energy sources powering such luminous nebulae like the Crab are believed to be young, energetic pulsars, i.e. extremely fast-rotating neutron stars with an age between ≈ 100 and $\approx 10\,000$ years. Pulsars are the remnants of massive stars which ended up in a core-collapse supernova. A good example for a PWN with a well detectable outer SNR shell is G21.5−0.9, as is shown in Fig. 2.1. In the case of G21.5−0.9, the pulsar with a

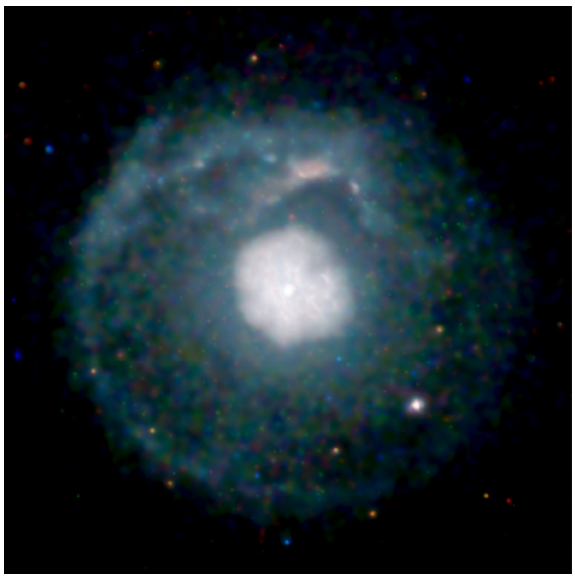

Fig. 2.1.: *Chandra image of the SNR G21.5−0.9. The central PWN with its pulsar is well distinguishable from the outer shell. Image taken from Matheson & Safi-Harb (2005).*

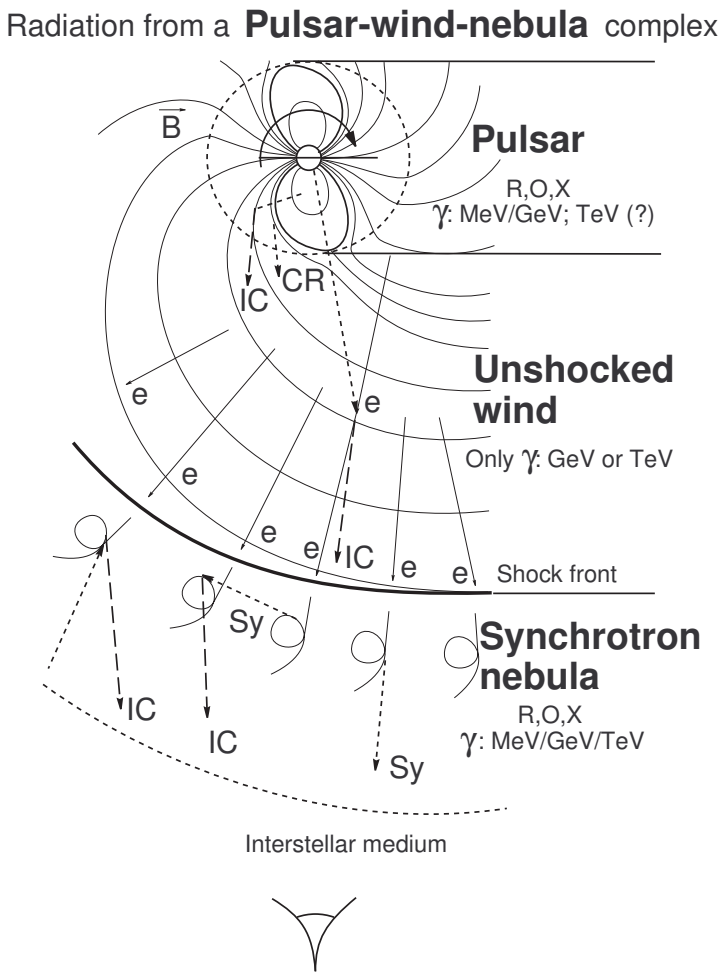

Fig. 2.2.: *Schematic view illustrating the radiation from different regions of a PWN. The dashed circle around the pulsar corresponds to its light cylinder. R (radio), O (optical) and X (X-ray) denote the emitted radiation in the individual areas, respectively. Image taken from Aharonian & Bogovalov (2003).*

rotation period of 61.8 ms was identified by Camilo et al. (2006) and corresponds to the point source visible in the center of Fig. 2.1.

Pulsars are assumed to continuously release part of their rotational energy as a lepton-dominated particle wind, which is called the pulsar wind (see also Fig. 2.2 for an illustration of the different stages of the pulsar wind). One quantity characterizing the nature of the outflow is the ratio of the Poynting flux and the particle energy flux (Gaensler & Slane 2006),

$$\sigma = \frac{F_{E\times B}}{F_{\text{particle}}}, \tag{2.1}$$

which is called the magnetization parameter. Close to the pulsar the outflow is dominated by $F_{E\times B}$ and thus $\sigma \gg 1$. In a PWN the ram pressure of the pulsar wind is in balance with the internal pressure of the PWN at the shock radius (Gaensler & Slane 2006)

$$R_{\text{S}} = \sqrt{\frac{\dot{E}}{4\pi\omega c P_{\text{PWN}}}}\,, \tag{2.2}$$

where $\dot{E}$ denotes the spin-down luminosity of the pulsar, ω the equivalent filling factor for an isotropic wind, and P_{PWN} the total pressure in the shocked nebular interior. Upstream this wind termination shock, the particles are not assumed to emit synchrotron radiation. At the shock, however, the properties of the pulsar wind change. The particles are shocked and reaccelerated, resulting in a domination of the particle flux downstream the termination shock and hence $\sigma \ll 1$. This part of the system corresponds to the actual PWN and is denoted as the *synchrotron nebula* in Fig. 2.2. In case of the Crab nebula, the termination shock is associated with the torus visible close to the pulsar in Fig. 1.1. Furthermore one can see two collimated jets which are emitted along the rotational axis of the pulsar.

2.1.2. Emitted Radiation

In the following, we are going to describe the radiation processes which give us the possibility to detect a PWN like G0.9+0.1 or the Crab nebula. Although there are several of such processes, in most PWNe with leptonic origin two of them are prevalent. These are presented in the following.

Synchrotron Radiation

A charged, relativistic particle that gets deflected by a magnetic field emits synchrotron radiation. Generally this can be understood as the Compton scattering of the particle off virtual photons from the magnetic field. For the case of an electron, Blumenthal & Gould (1970) derived the energy loss arising from this effect to

$$\left(\frac{\mathrm{d}E_{\mathrm{e}}}{\mathrm{d}t}\right)_{\mathrm{Sy}} = -\frac{2r_{\mathrm{e}}^2}{3c}\gamma^2 B^2 v^2 \sin^2\theta, \tag{2.3}$$

with $r_{\mathrm{e}} = 2.817 \times 10^{-13}\,\mathrm{cm}$ the classical electron radius and θ the pitch angle between the magnetic field and the particle's direction of motion. After averaging over θ, one obtains Eq. 5.27. When defining the critical frequency

$$\nu_{\mathrm{c}} = \frac{3eB\gamma^2}{4\pi m_{\mathrm{e}} c}\sin\theta, \tag{2.4}$$

the synchrotron energy loss for a single electron and a certain photon frequency is given by (Blumenthal & Gould 1970)

$$P_{\mathrm{Sy}}(\nu) = \frac{\sqrt{3}e^3 B\sin\theta}{mc^3}\,\frac{\nu}{\nu_{\mathrm{c}}}\int_{\nu/\nu_{\mathrm{c}}}^{\infty}\mathrm{d}\xi\,\mathrm{K}_{5/3}(\xi). \tag{2.5}$$

In this equation, $\mathrm{K}_{5/3}$ is a modified Bessel function of order 5/3. The next step is to find out the synchrotron emission from a power-law distribution of electrons. Assume an electron distribution of the following form:

$$N(\gamma) = k\gamma^{-p}N(\alpha)\frac{1}{4\pi}, \tag{2.6}$$

where the Lorentz factor is limited to $\gamma_1 < \gamma < \gamma_2$. k is assumed to be constant, and $N(\alpha)$ shall be chosen such that the whole equation reduces to $k\gamma^{-p}$ when having no pitch angle

dependence. The synchrotron emission from such a distribution of electrons is then given by (Blumenthal & Gould 1970)

$$P_{\mathrm{Sy}} = \left(\frac{\mathrm{d}W}{\mathrm{d}\nu \mathrm{d}t}\right)_{\mathrm{Sy}} = \frac{\sqrt{3}ke^3B}{4\pi m_{\mathrm{e}}c^2} \int \mathrm{d}\Omega_\theta \, N(\theta) \sin\theta \int_{\gamma_1}^{\gamma_2} \mathrm{d}\gamma \, \gamma^{-p} \frac{\nu}{\nu_c} \int_{\nu/\nu_c}^{\infty} \mathrm{d}\xi \, K_{5/3}(\xi). \tag{2.7}$$

This result can be simplified under the assumption that the γ range covers all electron energies, in particular $\nu_{c,1} \ll \nu$ and $\nu_{c,2} \gg \nu$. If furthermore the electrons are isotropically distributed, Eq. 2.7 becomes

$$\left(\frac{\mathrm{d}W}{\mathrm{d}\nu \mathrm{d}t}\right)_{\mathrm{Sy}} = \frac{4\pi k e^3 B^{(p+1)/2}}{m_{\mathrm{e}}c^2} \left(\frac{3e}{4\pi m_{\mathrm{e}}c}\right)^{(p-1)/2} a(p) \, \nu^{-(p-1)/2}, \tag{2.8}$$

where

$$a(p) = \frac{2^{(p-1)/2}\sqrt{3}\,\Gamma[(3p-1)/12]\,\Gamma[(3p+19)/12]\,\Gamma[(p+5)/4]}{8\pi^{1/2}(p+1)\Gamma[(p+7)/4]}. \tag{2.9}$$

Replacing ν by the related quantity $E = h\nu$, the spectral dependency of Eq. 2.8 becomes

$$\left(\frac{\mathrm{d}W}{\mathrm{d}E \mathrm{d}t}\right)_{\mathrm{Sy}} \propto E^{-(p-1)/2}. \tag{2.10}$$

When interested in the photon instead of the power spectrum, by using $\mathrm{d}W = E \, \mathrm{d}N$ this can be rewritten to

$$\left(\frac{\mathrm{d}N}{\mathrm{d}E \mathrm{d}t}\right)_{\mathrm{Sy}} \propto E^{-(p+1)/2}. \tag{2.11}$$

This means that for $\nu_{c,1} \ll \nu$ and $\nu_{c,2} \gg \nu$ the shape of the emitted synchrotron photon spectrum is a power law whose spectral index is related to that of the lepton spectrum by

$$\Gamma = \frac{p+1}{2}. \tag{2.12}$$

Fig. 2.3 shows the spectral energy distribution (SED) of the synchrotron radiation emitted by a lepton population following a power-law energy spectrum with $p = 2$, defined between 10^{11} and 10^{14} eV. The corresponding magnetic field strengths are 1, 10 and 100 μG, respectively. E.g. for the red curve, Eq. 2.12 is valid between $\approx 10^{-2}$ and 10^3 eV, yielding a spectral index of $\Gamma = 1.5$. Since in the figure the photon spectrum is multiplied with E^2, the slope in the logarithmic SED then corresponds to 0.5 in that energy range.

Inverse Compton Radiation

Another important physical process responsible for photon emission in PWNe is IC scattering. The usual Compton effect corresponds to an energy transfer from a photon to a resting or slowly moving charged particle. By contrast, the inverse Compton effect refers to the scattering of a relativistic charged particle off a photon with low energy. Generally both effects can be converted into each other by a Lorentz transformation. In astrophysics there are three major seed photon fields for IC scattering to be considered: Local starlight, infrared (IR) photons from local dust, and the photons of the cosmic microwave background (CMB). For sources with a high magnetic field, like e.g. the Crab Nebula, the IC scattering off synchrotron photons created in the source itself also plays an important role. This can, however, be firmly excluded for G0.9+0.1.

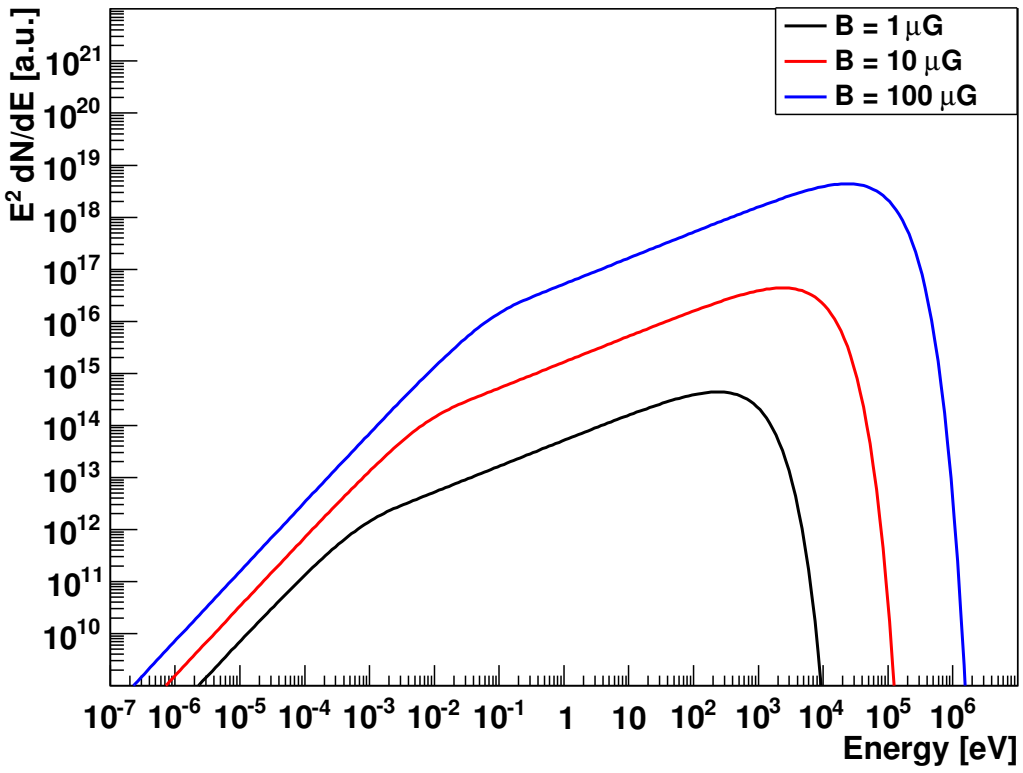

Fig. 2.3.: *Synchrotron emission of leptons following a power-law distribution for different magnetic field strengths.*

In the following, we again stick to the derivations of Blumenthal & Gould (1970). When the energy of the photon before scattering in the electron's rest frame is small compared to the rest energy of the electron, the cross section of the Compton effect equals the Thomson cross section

$$\sigma_{\mathrm{T}} = \frac{8\pi}{3} r_{\mathrm{e}}^2 = 6.65 \times 10^{-25}\,\mathrm{cm}^2. \tag{2.13}$$

For very energetic electrons, the situation gets more complicated and one has to use the cross section of Klein & Nishina (1929), as described in the following. Assume a photon gas with differential density

$$n(\varepsilon) = \frac{\mathrm{d}N_\varepsilon}{\mathrm{d}\varepsilon\,\mathrm{d}V}. \tag{2.14}$$

Given the initial Lorentz factor γ of the electron, the energy of the scattered photon, ε_1, can be related to the initial electron energy $\gamma m_{\mathrm{e}} c^2$ by introducing a dimensionless quantity E_1:

$$\varepsilon_1 = \gamma m_{\mathrm{e}} c^2 E_1. \tag{2.15}$$

Taking the Klein-Nishina cross section into account, Blumenthal & Gould (1970) derived the scattered photon spectrum for an electron to

$$\left(\frac{\mathrm{d}N_{\gamma,\varepsilon}}{\mathrm{d}t\mathrm{d}E_1}\right)_{\mathrm{IC}} = \frac{2\pi r_{\mathrm{e}}^2 m_{\mathrm{e}} c^3}{\gamma} \frac{n(\varepsilon)\mathrm{d}\varepsilon}{\varepsilon} \left[2q\ln q + (1+2q)(1-q) + \frac{1}{2}\frac{(\Gamma_{\mathrm{e}} q)^2}{1+\Gamma_{\mathrm{e}} q}(1-q)\right], \tag{2.16}$$

with $\Gamma_{\mathrm{e}} = 4\varepsilon\gamma/m_{\mathrm{e}}c^2$ and $q = E_1/\Gamma_{\mathrm{e}}(1-E_1)$.

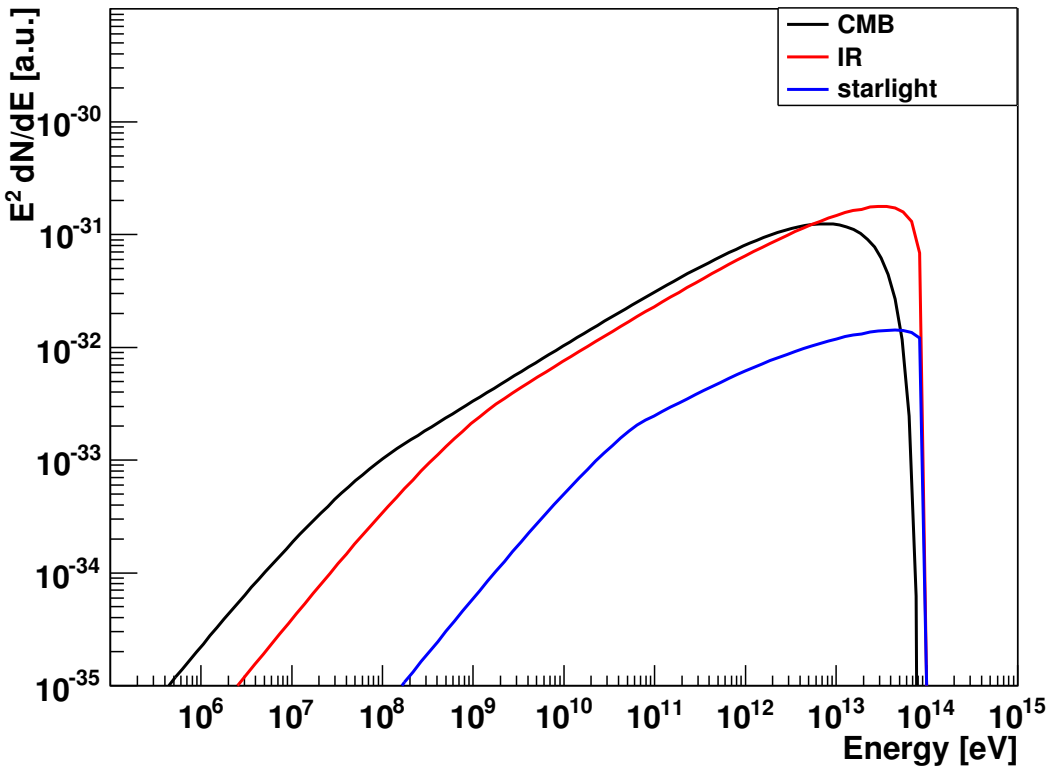

Fig. 2.4.: *IC scattering of a power-law-shaped lepton population. The lepton spectrum is the same as the one used for Fig. 2.3. The dust and starlight photon fields were taken from Porter & Strong (2005) for the case of G0.9+0.1 and an assumed distance of* 13 *kpc. For the CMB component a blackbody spectrum was used.*

Knowing the differential scattered photon spectrum for a specific initial lepton and photon energy, we are now able to calculate the total IC spectrum. Let the differential number of electrons be $\mathrm{d}N_\mathrm{e} = N_\mathrm{e}(\gamma)\mathrm{d}\gamma$. The photon spectrum is then given by the integration of Eq. 2.16 over ε and γ (Blumenthal & Gould 1970):

$$\left(\frac{\mathrm{d}N_\mathrm{tot}}{\mathrm{d}t\mathrm{d}\varepsilon_1}\right)_\mathrm{IC} = \int\int N_\mathrm{e}(\gamma)\mathrm{d}\gamma \left(\frac{\mathrm{d}N_{\gamma,\varepsilon}}{\mathrm{d}t\mathrm{d}\varepsilon_1}\right)_\mathrm{IC}. \tag{2.17}$$

Fig. 2.4 shows a SED obtained when scattering a power-law-shaped lepton population on different photon fields. The lepton spectrum is the same as the one used for Fig. 2.3. For the dust and starlight components, we used the fields from Porter & Strong (2005) (see also Section 5.7.1) at the location of G0.9+0.1 and a distance of 13 kpc. For the CMB photon field we adopted a blackbody distribution with $T = 2.725\,\mathrm{K}$ and an energy density of $4.20 \times 10^{-13}\,\mathrm{erg/cm^3}$.

Similar to the case of synchrotron radiation, the integration can be analytically solved for a power-law distribution of electrons

$$N_\mathrm{e}(\gamma) = K_\mathrm{e}\gamma^{-p}, \tag{2.18}$$

defined between γ_0 and γ_m. The seed photon field shall follow a blackbody distribution:

$$n(\varepsilon) = \frac{1}{\pi^2(\hbar c)^3} \frac{\varepsilon^2}{e^{\varepsilon/kT} - 1}. \tag{2.19}$$

When just looking at the part of the spectrum where $\frac{1}{2}(\varepsilon_1/\varepsilon)^{1/2} > \gamma_0$ and $\frac{1}{2}(\varepsilon_1/\varepsilon)^{1/2} \ll \gamma_m$, Eq. 2.17 simplifies to (Blumenthal & Gould 1970)

$$\left(\frac{\mathrm{d}N_{\mathrm{tot}}}{\mathrm{d}t\mathrm{d}\varepsilon_1}\right)_{\mathrm{IC}} = \frac{r_{\mathrm{e}}^2}{\pi\hbar^3c^2} K_{\mathrm{e}} (kT)^{(p+5)/2} F(p) \varepsilon_1^{-(p+1)/2}, \tag{2.20}$$

with

$$F(p) = 2^{p+3} \left[(p^2 + 4p + 11)/(p+3)^2(p+1)(p+5)\right] \Gamma[1/2(p+5)]\, \zeta[1/2(p+5)]. \tag{2.21}$$

In the last equation, ζ denotes the Riemann function. As can be seen in Eq. 2.20, a power-law electron distribution with spectral index p results in a power-law photon spectrum with index $(p+1)/2$. Notably this is exactly the same relation as for the synchrotron radiation (Eq. 2.12). This can be understood by recalling that both effects are closely related to each other, as already mentioned before.

2.2. G0.9+0.1 and its Central Pulsar Wind Nebula

The nomenclature of G0.9+0.1 expresses its direction in the sky, the G standing for the galactic coordinate system and the two numbers giving the longitude and latitude in degrees, respectively. Therefore one can easily see that G0.9+0.1 is located less than one degree in projection from the galactic center (GC). The first detection of G0.9+0.1 was reported by Kesteven (1968). In the reference the author presents a catalogue of galactic radio sources, detected with the Molonglo radio telescope. According to Helfand & Becker (1987), the overall radio morphology of G0.9+0.1 is dominated by a luminous core with a diameter of $\approx 2'$ surrounded by a fainter, but still well detectable shell (diameter $\approx 8'$), identifying the source as a composite SNR (see also Fig. 2.5).

The first solid detection of G0.9+0.1 in X-rays was performed with the *BeppoSAX* satellite (Mereghetti et al. 1998). A newer on-axis observation performed with the same instrument allowed Sidoli et al. (2000) to prove the non-thermal origin of the radiation. As the best-fit result the authors present a power law with a spectral index of $\Gamma = 2.0 \pm 0.3$ (with $\frac{\mathrm{d}N}{\mathrm{d}E} \propto E^{-\Gamma}$) and a column density of $n_{\mathrm{H}} = (1.0 \pm 0.2) \times 10^{23}\,\mathrm{cm}^{-2}$. The derived unabsorbed energy flux in the $2-10\,\mathrm{keV}$ band is $(6.6^{+1.3}_{-0.8}) \times 10^{-12}\,\mathrm{erg\,s^{-1}\,cm^{-2}}$. Follow-up observations with *Chandra* (Gaensler et al. 2001) and *XMM-Newton* (Porquet et al. 2003) unambiguously identified the core of the SNR as a PWN. The morphology of G0.9+0.1 seen with the *Chandra* dataset (see Fig. 2.6) suggests an axial symmetry with an angle of $\approx 165°$, measured counterclockwise from north (Gaensler et al. 2001). Along the symmetry axis, approximately 10 arcseconds south of the region of brightest emission, lies an unresolved source (CXOU J174722.8−280915). It was detected with a signal-to-noise ratio of $\approx 4\,\sigma$ and most likely corresponds to the pulsar itself, but this has not been confirmed yet (further discussion in Section 2.3). The authors also observe a semicircular arc with a radius of $25-30$ arcseconds and an elongated jetlike feature of length $35-40$ arcseconds. They propose these features as candidates for the torus representing the wind termination shock and a jet caused by the pulsar. Notably this would lead to an extremely large

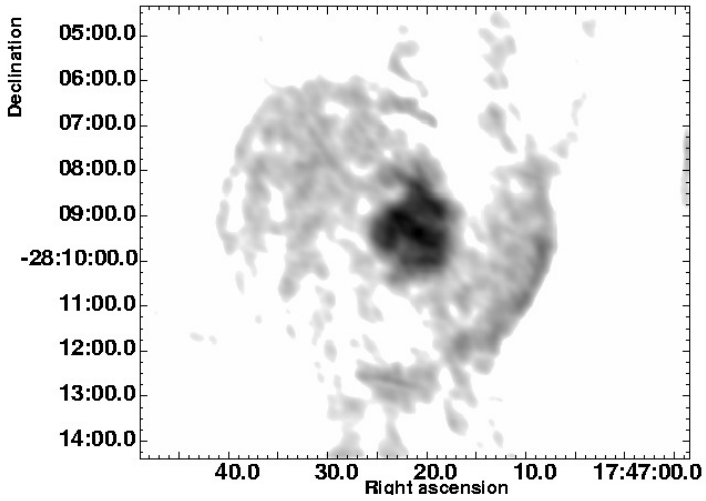

Fig. 2.5.: *VLA radio image of the whole SNR at $\lambda = 20\,\mathrm{cm}$. The core corresponding to the PWN is prominent in contrast to the outer shell. Image taken from Dubner et al. (2008).*

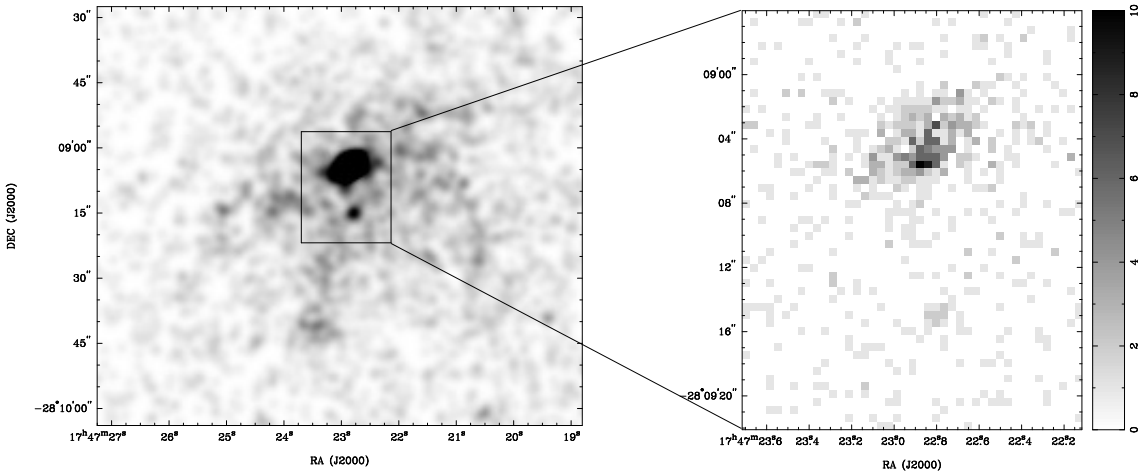

Fig. 2.6.: *Left: Smoothed skymap showing the inner region of the G0.9+0.1 PWN as seen by the Chandra telescope. Right: Unsmoothed countmap containing the region of brightest emission as well as the point-like source CXOU J174722.8−280915 to the south. Figure from Gaensler et al. (2001).*

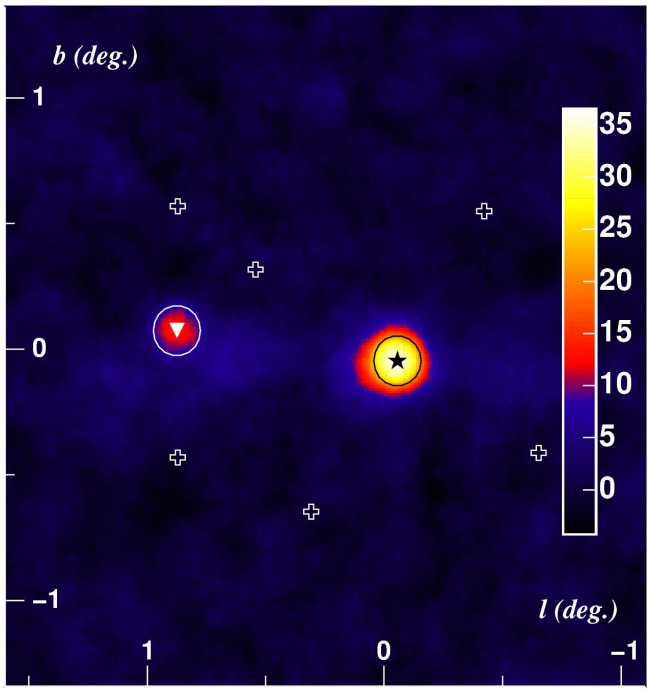

Fig. 2.7.: *H. E. S. S. significance map showing the region around the GC. The position of Sgr A* is denoted with a star, the one of G0.9+0.1 with a triangle. The white crosses mark the telescope pointing positions of the observations. Figure taken from Aharonian et al. (2005).*

shock radius of at least 1 pc when assuming a distance to the object of more than 8.5 kpc (distance discussed in Section 2.3).

Porquet et al. (2003) extensively analyzed the first *XMM-Newton* data set of G0.9+0.1 (further information in Section 4.1). Due to the high sensitivity of *XMM-Newton* they were able to detect faint X-ray emission from the shell of the SNR. The already mentioned source CXOU J174722.8−280915 is also distinguishable from the diffuse PWN emission in an energy band of $6 - 12$ keV despite the larger point spread function of *XMM-Newton* compared to *Chandra*. Separately analyzing different regions in the PWN, Porquet et al. (2003) observe a positive gradient in the spectral index from east to west. This is interpreted as fast rotation with resultant Doppler boosting of the leptons which constitute the PWN.

Dubner et al. (2008) compared newer radio observations with a revised *XMM-Newton* analysis. These authors show that the X-ray PWN almost fills the size of the radio core, which indicates a moderate magnetic field (see e.g. Gaensler & Slane 2006). Dubner et al. (2008) support the axial symmetry suggested by Gaensler et al. (2001), but do not see any spectral variations in the radio regime as reported by Porquet et al. (2003). Furthermore, the authors do not find a radio counterpart of CXOU J174722.8−280915.

G0.9+0.1 has also been observed by H. E. S. S. (Aharonian et al. 2005) in VHE γ-rays above 200 GeV. The detected signal is very faint, but due to the large field of view of H. E. S. S., the telescopes simultaneously observed G0.9+0.1 when pointing towards the GC, resulting in a high significance of $13\,\sigma$ due to the high exposure. Fig. 2.7 shows the significance map presented in that paper. For H. E. S. S., the source appears point-like, with an upper limit on the intrinsic extension between $1.3'$ assuming a Gaussian emission

region and $2.2'$ for the emission from a thin shell (both 95 % confidence level). The VHE γ-ray spectrum is well fitted by a power law with a spectral index of 2.29 ± 0.14 and a photon flux of $(5.5 \pm 0.8) \times 10^{-12}\,\mathrm{cm}^{-2}\,\mathrm{s}^{-1}$ above 200 GeV, making G0.9+0.1 the faintest H. E. S. S. source detected at that time.

2.3. The Pulsar PSR J1747−2809 and the Distance Problem

In 2009, Camilo et al. discovered PSR J1747−2809, the pulsar powering G0.9+0.1, using the NRAO Green Bank Telescope at a frequency of 2 GHz. The detected signal is strongly scattered and absorbed, with a positional uncertainty of $3'$ and a corrected dispersion measure of DM $= (1133 \pm 3)\,\mathrm{pc\,cm}^{-3}$. The pulsar has a rotation period of $P = 52$ ms. The derived pulsar properties from the two analyzed observations are $\tau_c = 5.3\,\mathrm{kyr}$[1] and $\dot{E} = 4.3 \times 10^{37}\,\mathrm{erg/s}$. Notably this corresponds to the second highest known spin-down luminosity of galactic pulsars, only surpassed by the Crab pulsar. Revealing the similarities between the system of PSR J1747−2809/G0.9+0.1 and PSR J1833−1034/G21.5−0.9, Camilo et al. (2009) consider the true age of PSR J1747−2809 well below τ_c, as was already shown for PSR J1833−1034. The authors estimate the true age of the system at $2 - 3$ kyr.

Unfortunately, the mentioned positional uncertainty neither proves nor disproves that CXOU J174722.8−280915 is the X-ray counterpart of PSR J1747−2809. Due to the high absorption and hard spectrum, Gaensler et al. (2001) ruled out the possibility that this point-like source corresponds to a foreground star. Given the fact that the probability of its emission being originated from a background active galactic nucleus is only $\approx 10^{-2}$, the authors deem the source belonging to the PWN. Although it cannot be excluded that PSR J1747−2809 is actually located in the region of brightest emission well visible in Fig. 2.6, CXOU J174722.8−280915 is definitely its best candidate.

Up to the present, the distance to this PWN is not constrained very well. The considerably high absorption column density points to a distance of ≈ 10 kpc or higher (as outlined e.g. in Gaensler et al. 2001). Nevertheless some authors (for example Aharonian et al. 2005; Dubner et al. 2008) adopt $d = 8.5$ kpc, which would imply G0.9+0.1 lying in the direct vicinity of the GC. Applying the NE2001 electron model (Cordes & Lazio 2002) to the dispersion measure of PSR J1747−2809, Camilo et al. (2009) obtain $d \approx 13$ kpc, but admit that this model could be substantially in error for sources toward the inner Galactic regions. Due to this error, they propose an approximate distance between 8 and 16 kpc, leaving this problem unsolved.

[1] $\tau_c = P/(2\dot{P})$ is the characteristic age of a pulsar and is an estimation of its real age when assuming $P_0 \ll P$ (Gaensler & Slane 2006).

3. The *XMM-Newton* Satellite

The earth's atmosphere is not transparent for X-rays in the keV energy range. Therefore it is not possible to detect and examine celestial X-ray sources from the ground, making the use of satellites inevitable for covering that energy range. In this work, the data of a current imaging X-ray satellite, *XMM-Newton* (X-ray Multi-Mirror Mission, Jansen et al. 2001), is used. This satellite is presented in the following.

3.1. The Satellite

The *XMM-Newton* satellite was launched on board the *Ariane V504* rocket by the European Space Agency (ESA) on December 10th, 1999. With a mass of approximately four tons and a length of $\approx 10\,\mathrm{m}$, *XMM-Newton* is the largest scientific satellite launched by the ESA up to now. Its orbit is highly eccentric, with a perigee of $\approx 7\,000\,\mathrm{km}$ and an apogee of $\approx 114\,000\,\mathrm{km}$. The satellite's revolution period is about two days. *XMM-Newton*'s large orbit is also hinted at in the artistic view shown in Fig. 3.1. The spacecraft carries three

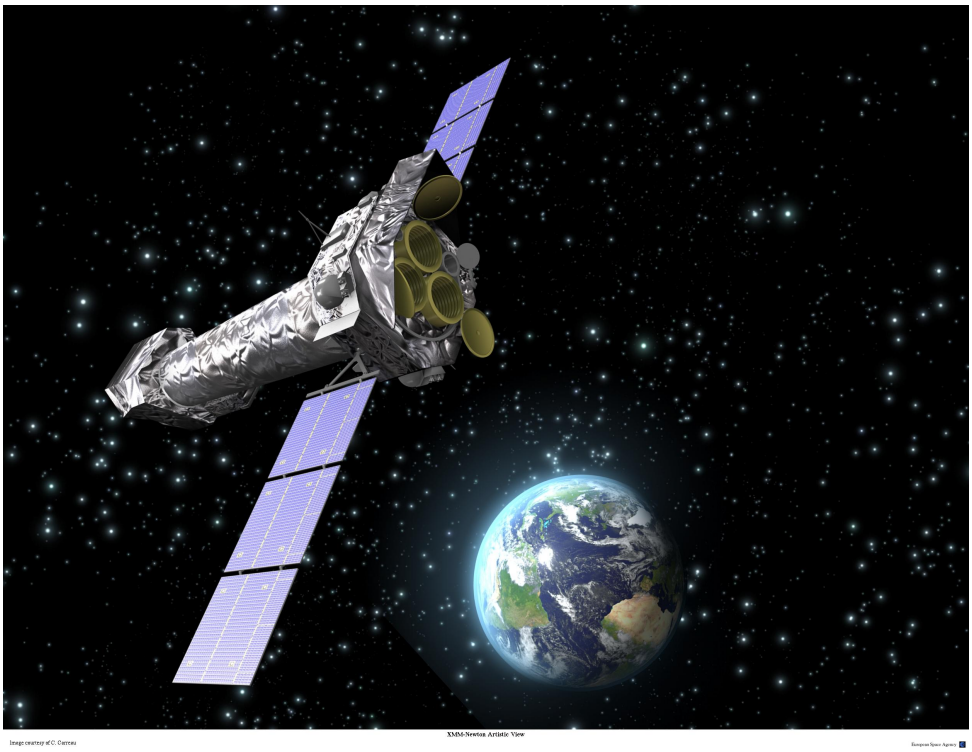

Fig. 3.1.: *Artistic view of the XMM-Newton satellite. Visible are the three X-ray telescopes as well as the optical monitor (the latter in grey). Image by ESA/XMM-Newton.*

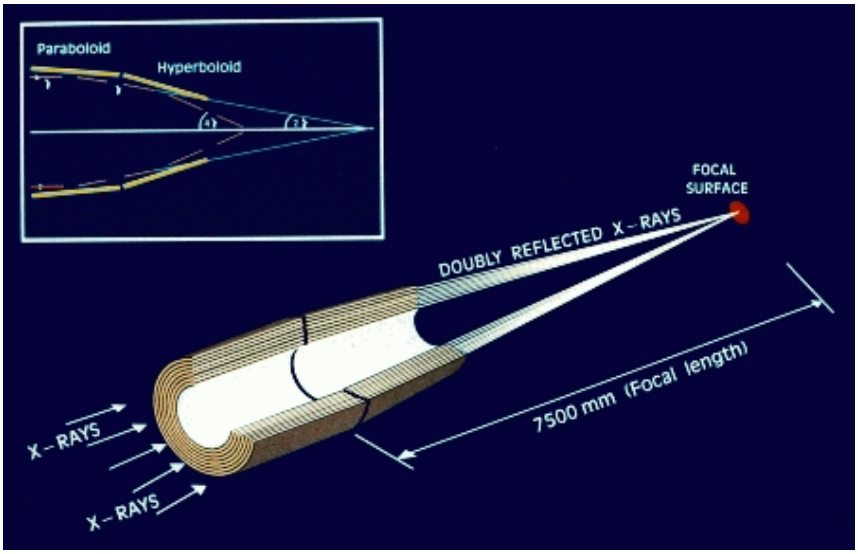

Fig. 3.2.: *Schematic view of the light path for one of XMM-Newton's X-ray telescopes. Image by ESA/XMM-Newton.*

X-ray telescopes as well as an optical monitor and two star trackers.

3.2. The X-ray Telescopes

XMM-Newton was mainly designed to detect and image celestial sources with a low surface brightness in the energy range $0.1 - 10\,\mathrm{keV}$. Its centerpieces designed for that purpose are the X-ray telescopes, which are described in the following.

3.2.1. Mirrors

The optical part of each of the three telescopes is identical, mainly consisting of 58 Wolter-type I grazing-incidence mirrors (Wolter 1952), which are cofocally and coaxially arranged. Each of these mirrors consists of a paraboloid and a hyperboloid, leading to a double reflection to focus X-rays as indicated in Fig. 3.2. The diameters of the mirrors range from 306 to 700 mm and their thickness from 0.47 to 1.07 mm, respectively. The minimum distance between adjacent mirrors is 1 mm. The substrate material is nickel, and each of the mirrors is coated with gold to achieve a high reflectivity. Using the grazing-incidence focusing technique requires quite a large focal length of 7 500 mm in the case of *XMM-Newton*. The width of the on-axis point spread function (PSF) lies between 4.2 and 6.6 arcseconds, depending on the instrument and the photon energy. The field of view (FoV) of each telescope has a diameter of approximately $30'$.

In the case of a Wolter telescope, the effective area is not simply given by the diameter of the telescope, but also by the number of mirrors nested in the telescope. *XMM-Newton* was specially designed for achieving a high sensitivity in order to observe extended sources with low surface brightness. Therefore optimizing the effective area in the whole keV range was a major goal for that observatory, resulting in the combination of 58 mirrors with the mentioned specifications.

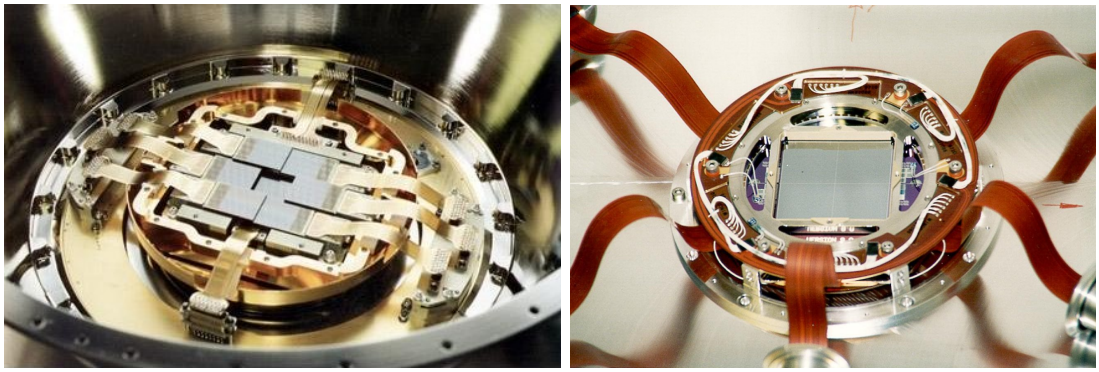

Fig. 3.3.: *Left: CCDs of one of the MOS cameras. Right: CCDs of the pn camera. Both images are from ESA/XMM-Newton.*

The effective area for the imaging mode of two of the telescopes (the ones with the MOS cameras, see description below) is decreased by about 56 % with respect to the third one since they are equipped with a reflection grating array (RGA), deflecting a certain part of the radiation to a separate camera[1].

In order to reject stray light and low-energy electrons, the telescopes are equipped with optical and X-ray baffles as well as an electron deflector, respectively.

3.2.2. Cameras

The next important units to be described are the cameras of the telescopes. *XMM-Newton* is equipped with two different EPIC (European photon imaging camera) camera types which are introduced in the following two paragraphs.

The MOS Cameras

The first camera type used in two of the telescopes is the so-called MOS camera (Turner et al. 2001). Each MOS camera consists of 7 front-illuminated CCDs (Short et al. 1998) as shown in the left panel of Fig. 3.3. The central CCD is set into the focus on the optical axis. In order to correct for the curvature of the focal plane, the other CCDs are stepped towards the mirrors by 4.5 mm. Each CCD has a size of $2.5 \times 2.5\,\mathrm{cm}^2$ and consists of 600×600 pixels, with one pixel covering $1.1 \times 1.1\,\mathrm{arcsec}^2$ in the FoV. Due to absorption in the electrode structure, the low-energy response of the front-illuminated MOS-CCDs is decreased with respect to the one of the back-illuminated pn-CCDs (see next paragraph).

The cameras can be operated in different modes. In case of MOS, the outer 6 chips always work in the so-called standard full frame mode where all pixels are read out. In addition to that mode, the central CCD can also be operated in the partial window or in the timing mode. Whereas in the partial window mode only a part of every chip is read out, the timing mode just provides a one-dimensional image resolution since the rows are read out at high speed, hence providing a higher time resolution.

[1] Data from the RGAs were not used for this work and therefore these instruments are not further described. For more information, the reader is referred to den Herder et al. (2001).

The two MOS cameras are oriented orthogonally to each other, with the advantage of mutual coverage of the CCD gaps.

The pn Camera

The third of the X-ray telescopes is equipped with a detector specifically developed for *XMM-Newton*, the pn camera (Strüder et al. 2001). It consists of twelve pn-CCDs which are arranged in four quadrants, produced on a single wafer (see the right panel of Fig. 3.3). Each of the $3 \times 1\,\mathrm{cm}^2$ CCDs has 200×64 pixels, where a single pixel corresponds to $4.1 \times 4.1\,\mathrm{arcsec}^2$. The photons reach the detector from the rear side and produce electron-hole pairs, which are separated by electric fields and read out afterwards.

The whole pn array can be operated in several modes. Similar to the standard full frame mode, there is also the extended full frame mode where the integration time is higher, leading to less out-of-time events. This mode is well suited for non-variable extended sources with low surface brightness. In addition, several partial window and timing modes are available.

In order to prevent IR, visible and UV photons from reaching the detectors, each camera includes several filters in order to reduce such noise. Depending on the source and the strength of the noise, the cameras can be operated with thin, medium or thick filters. Alternatively, it is also possible to use a total blocking filter or no filter at all.

3.3. Optical Monitor

In order to cover a wider energy range, the spacecraft is also equipped with a 30 cm Ritchey-Chretien optical und UV telescope, called the optical monitor (OM). Since no data from the OM was used in this work, this instrument is not further described in this context. For a detailed review, the reader is referred to Mason et al. (2001).

4. X-rays from G0.9+0.1

In the previous Chapter, the *XMM-Newton* telescope has been characterized as an X-ray detector with a very high effective area. This characteristic makes it well suited for the analysis of extended sources with low surface brightness like G0.9+0.1. In the following, the *XMM-Newton* analysis performed on this object is described in detail. Afterwards we present the spectra of four annulus-shaped extraction regions.

4.1. Observations

G0.9+0.1 has been observed on-axis twice in 2000 and 2003 by the *XMM-Newton* telescope. Table 4.1 lists the properties of these two observations analyzed in this work. There is also a third data set available (Observation ID (OID): 0205240101), but the high off-axis position of approximately $12'$ makes a spatially resolved spectral analysis difficult due to the strong distortion of the PSF at large off-axis angles. For this reason, this observation was excluded from our analysis. The earlier data set (OID: 0112970201) has already been extensively analyzed by Porquet et al. (2003, see Section 2.2). During both on-axis observations, the medium filter was used for the EPIC-MOS and EPIC-pn cameras. The MOS cameras were operated in the standard full frame mode in both cases, whereas the pn camera was operated in the extended full frame mode (2000) and in the large window mode (2003).

4.2. Data Analysis

We analyzed the data using version 9.0.0 of the Science Analysis System (SAS) provided by the *XMM-Newton* Science Operations Centre, together with tools from the FTOOLS package (Blackburn 1995). In order to reduce the influence of soft proton flaring, good time intervals (GTI) were selected by applying a maximum count threshold to the high

Table 4.1.: *Analyzed G0.9+0.1 XMM-Newton observations.*

Observation ID	Instrument EPIC	Exposures (ks) performed[(1)]	net[(2)]
0112970201	pn	11.7	11.3
0112970201	MOS1/2	17.2	17.2
0144220101	pn	43.7	26.9
0144220101	MOS1	49.4	44.1
0144220101	MOS2	49.4	45.3

[(1)] Before background screening
[(2)] After background screening

energy lightcurve ($7-15\,\mathrm{keV}$) obtained with the standard analysis chain. As the pn camera is more sensitive than the two MOS cameras, it is reasonable to choose different thresholds. Values of 8 respectively 2 background counts per second were chosen for the pn and for the two MOS cameras. The resulting net exposures are also shown in Table 4.1. Evidently, the newer observation suffers from strong flare losses. Still the remaining net exposure easily surpasses the one of the older observation, leading to well increased statistics allowing to perform a spatially resolved analysis as required for the modeling (see Chapter 5). For each data set, only good (FLAG = 0) single and multiple (PATTERN ≤ 4 for pn and ≤ 12 for MOS) events were selected. Since the source is extended and has a moderate surface brightness, it is not necessary to correct for pile-up. In order to take into account the vignetting of the telescopes, the weighting method introduced by Arnaud et al. (2001) was applied, which is explained in the following paragraph according to the description in the reference. We implemented this method to replace the standard SAS spectral extraction routine.

Weighting Method The effective area of the *XMM-Newton* telescopes is a function of the photon energy and the distance from the instrument's optical axis. For an exact spectral modeling one needs a spatially and spectrally resolved model of the observed region. This model then has to be convolved with the instrument response, and the resulting spectrum compared with the measured one. Implementing this method is difficult and it can only be used if a reliable spatially resolved model is available.

The standard strategy is to use the emission-weighted effective area calculated from the observed photon distribution and take the same area for all photon energies. The model spectrum can then be compared with the observed spectrum unfolded with this effective area. Unfortunately, this method has two major disadvantages. The first one is a bias introduced by using the counts of the observed spectrum, which are intrinsically more pronounced at the center because of the higher effective area. This means that the influence of these central regions is overestimated. Secondly, the procedure neglects the fact that the decrease of the effective area to the outer regions is energy-dependent.

Arnaud et al. (2001) suggest the following, alternative method. A photon with energy E_I detected at the position (x_j, y_j) has the effective area $A_{x_j,y_j}(E_I)$, in contrast to the effective area at the center[1], $A_{0,0}(E_I)$. The photon count is weighted as shown in the following equation:

$$w_j = \frac{A_{0,0}(E_I)}{A_{x_j,y_j}(E_I)}. \tag{4.1}$$

When extracting the spectrum of a region *Reg*, all photon counts of that region belonging to a certain energy channel I are weighted with the appropriate factor and summed up to obtain the corrected spectrum $C(I)$:

$$C(I) = \sum_j w_j\,; \qquad (x_j, y_j) \in Reg \tag{4.2}$$

with

$$E_I - \Delta E_I/2 < E_j < E_I + \Delta E_I/2. \tag{4.3}$$

Note that the error estimate also has to be modified:

$$\sigma^2(C(I)) = \sum_j w_j^2. \tag{4.4}$$

[1]Note that this refers to the focus of the particular telescope, not the center of the detector.

$C(I)$ is an estimation of a spectrum one would obtain with a flat detector. It can thus be compared with a model spectrum of the region convolved with the detector response at the telescope's focus. In the case of *XMM-Newton*, the only drawback is a slight increase in the statistical error by a factor of $\sqrt{\langle w_j^2 \rangle}/\langle w_j \rangle$.

For extended sources with low surface brightness like G0.9+0.1, a proper treatment of all background components is of particular importance. For this reason the method for particle background subtraction of Majerowicz et al. (2002) was used for the analysis. In the following this method is outlined as described in the reference.

Particle Background Subtraction After having rejected the flare component by identifying the GTI, two essential background components remain. The first one is the astrophysical X-ray background. Its treatment in this analysis is described after this paragraph. The second component mainly originates in cosmic rays passing through the satellite and depositing a part of their energy in the detector, in addition to detector noise and other non-X-ray background. The influence of this background component is well known due to high-exposure observations taken with a closed filter. These observations are provided by David Lumb[2] for every EPIC instrument and operation mode. In this method, event lists of the particle observation are created for the same detector region as for the source observation. For a correct normalization between both observations, the count rates are compared in the high energy band where the telescopes are not sensitive to X-ray photons any more. For this analysis, the energy bands of $12 - 14\,\mathrm{keV}$ for the pn and $10 - 14\,\mathrm{keV}$ for each MOS camera were chosen. After checking that the count rates are comparable between source and particle observation, the particle spectrum is subtracted both from the source and from the infield background spectra.

The following list describes the approach to the spectral analysis for each camera and observation after the FLAG, PATTERN and GTI filtering as carried out in this work:

- To account for the astrophysical background component, an infield background located near the source and on the same CCD chip is defined.
- For both the source and the infield background region, corresponding particle event lists are created for the same detector regions, as described above.
- Then the described weighting method is applied to all these event lists, creating spectral files.
- Finally, the counts from the spectra of the particle observations are subtracted from the corresponding spectra of the source and infield background observations, normalized by the ratio of the high energy countrates (see explanation above). As a result one obtains two files, a spectrum of the source region and one of the infield background region, both corrected for the particle background.

Note that in the third step, the weighting method is also applied to the particle event lists, although the particle background is not affected by the vignetting effect. This is done because at this stage of the analysis, the particle component is still contained in the source and infield background event lists and therefore is also scaled up by the weighting method.

[2]The files are available from the following site: ftp://xmm.vilspa.esa.es/pub/ccf/constituents/extras/

A widely used method to group data from individual energy channels is to require a minimum number of counts from the source region per energy bin in the spectrum. In the case of a highly absorbed extended source like G0.9+0.1, this approach is quite inadequate since especially in the low energy domain a great part of the counts from the source region is actually due to astrophysical background. Instead we implemented a method which bins the spectra such as to achieve a certain signal-to-noise ratio (see e.g. Li & Ma (1983), albeit suggested for γ-ray astronomy in that publication). The following derivation follows the explanation of these authors, yet it is adapted to the needs of X-ray astronomy.

Significance Binning Let N_{on} be the number of counts (or weighted counts when using the described method of Arnaud et al. (2001)) contained in a certain energy range of the spectrum of the source region, and N_{off} the counts in the same range of the infield background region spectrum file. The number of excess counts N_{S} is then given by

$$N_{\mathrm{S}} = N_{\mathrm{on}} - \alpha N_{\mathrm{off}} \tag{4.5}$$

with $\alpha = A_{\mathrm{on}}/A_{\mathrm{off}}$ the ratio of the *backscale*[3] values of these two regions, assuming that the exposure time is identical for both. As the regions are separated, N_{on} and N_{off} are not correlated. This means that the variance of N_{S} is

$$\sigma^2(N_{\mathrm{S}}) = \sigma^2(N_{\mathrm{on}}) + \sigma^2(\alpha N_{\mathrm{off}}) = \sigma^2(N_{\mathrm{on}}) + \alpha^2\sigma^2(N_{\mathrm{off}}) \tag{4.6}$$

and therefore the standard deviation can be estimated as

$$\hat{\sigma}(N_{\mathrm{S}}) = \sqrt{\hat{\sigma}^2(N_{\mathrm{on}}) + \alpha^2\hat{\sigma}^2(N_{\mathrm{off}})} = \sqrt{N_{\mathrm{on}} + \alpha^2 N_{\mathrm{off}}}\,. \tag{4.7}$$

Then the significance (or signal-to-noise ratio) S reads:

$$S = \frac{N_{\mathrm{S}}}{\hat{\sigma}(N_{\mathrm{S}})} = \frac{N_{\mathrm{on}} - \alpha N_{\mathrm{off}}}{\sqrt{N_{\mathrm{on}} + \alpha^2 N_{\mathrm{off}}}}\,. \tag{4.8}$$

Throughout this work, channels are grouped to a minimum value of $S = 5$ per bin in the spectra. For the pn as well as for each MOS camera, the width of one energy channel is well below the energy resolution of the detector. Since it is not very useful to admit a spectral bin narrower than an instrument's energy resolution, we required as an additional threshold a minimum number of channels. The average energy resolution for both pn and MOS is $\approx 150\,\mathrm{eV}$. The width of one channel is $5\,\mathrm{eV}$ ($15\,\mathrm{eV}$) for pn (MOS), so the chosen minimum value equals 30 (10) channels, respectively.

4.3. Extraction Regions

We extracted spectra of four annuli centered on the position of CXOU J174722.8−280915, which is the best candidate for PSR J1747−2809, as outlined in Section 2.3. These regions are illustrated in Fig. 4.1, a smoothed *XMM-Newton* count map of G0.9+0.1, merged from exactly the same data as taken for the spectral analysis. This map has been generated using the *SAOImage ds9* tool (Joye & Mandel 2003). The properties of the annuli are given in Table 4.2. The annuli are numbered with increasing distance to CXOU J174722.8−280915.

[3] The *backscale* value of an extraction region corresponds to the number of active CCD pixels and is thus proportional to its solid angle.

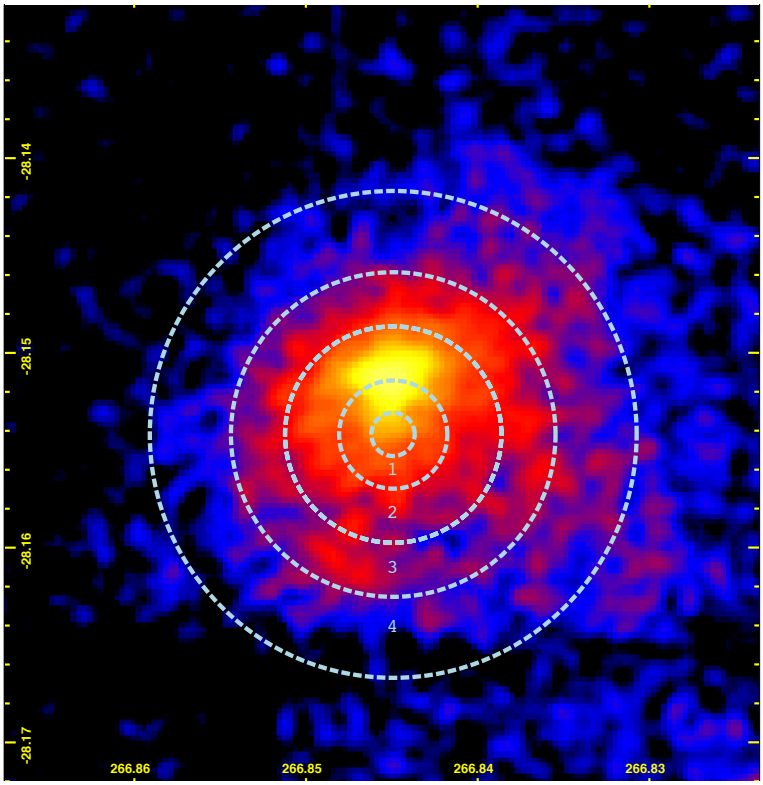

Fig. 4.1.: *Smoothed XMM-Newton count map merged from the MOS and pn data of the 2000 and 2003 observations (see Table 4.1). The annuli chosen for the spectral analysis are shown in grey (properties listed in Table 4.2). The dark region at the southern edge of the outermost annulus corresponds to a CCD border of the pn data from the 2003 observation.*

Since the appearance of G0.9+0.1 in X-rays obviously deviates from radial symmetry at least at higher angular distances, we refrained from extracting spectra with greater radii. Fortunately, for each observation and camera, the observed part of the source covered only a single CCD, which does not further complicate the spectrum extraction. Nevertheless it has to be mentioned that a small part of the fourth annulus lapped into the CCD border region for the pn data of the 2003 observation (see Fig. 4.1). However, the influence of this effect is considered negligible.

For the spectral modeling, we used version 12.5.0 of the XSPEC tool (Arnaud 1996). The extracted spectra for each of the four annuli were fitted in parallel with an absorbed power-law model. We used the *tbabs* absorption model, along with the abundances of the interstellar medium from Wilms et al. (2000). Given that, apart from the photon index, we are primarily interested in the unabsorbed energy flux of each region (described in detail in Chapter 5), we convolved the spectrum model with the *cflux* command. This has the particular advantage of a simpler and more accurate error estimation of that value. The model expression for XSPEC then is TBABS*CFLUX*PO.

Table 4.2.: *Properties of the XMM-Newton annuli chosen for the spectral analysis.*

Annulus No.	Radius (arcsec) inner	outer
1	4	10
2	10	20
3	20	30
4	30	45

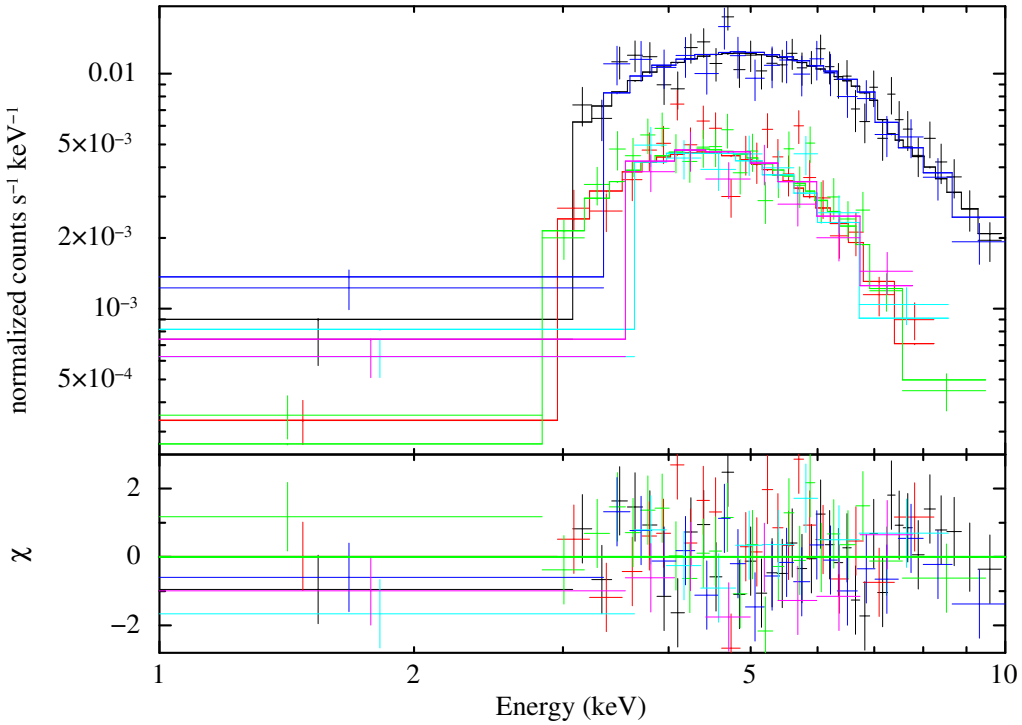

Fig. 4.2.: *Energy spectrum extracted from the second annulus. The dark blue and black curves correspond to the pn camera of the 2000 and 2003 observations. The four lower curves represent MOS1/2 of both observations. The data were fitted in parallel with an absorbed power-law model. The spectra of all annuli are contained in Appendix A.*

Table 4.3.: *Results obtained by fitting a power-law spectrum to the XMM-Newton data of G0.9+0.1.*

Annulus No.	Γ	Unabsorbed Flux$^{(*)}$ (10^{-12} erg cm^{-2} s^{-1})	Surface Brightness (10^{-16} erg cm^{-2} s^{-1}arcsec^{-2})	χ^2/dof
1	1.46 ± 0.17	0.50 ± 0.02	19.0 ± 0.9	45/55
2	1.65 ± 0.10	1.28 ± 0.03	13.7 ± 0.4	131/120
3	1.90 ± 0.12	1.10 ± 0.03	7.1 ± 0.2	85/95
4	2.18 ± 0.13	1.13 ± 0.04	3.4 ± 0.1	72/79

$^{(*)}$ Energy range $2.5 - 10$ keV

4.4. X-ray Spectra

In order to obtain a statistically significant value for the absorption column density, we first fitted the spectrum of a circle with a radius of 45 arcseconds, equaling the outer radius of the fourth annulus, in the energy range $2 - 10$ keV. The circle was also centered on CXOU J174722.8−280915. The result is $n_{\mathrm{H}} = (2.26 \pm 0.15) \times 10^{23}\,\mathrm{cm}^{-2}$. Due to the different abundances used in our fit, this value is considerably higher compared to the one obtained by Porquet et al. (2003, $n_{\mathrm{H}} = (1.39 \pm 0.13) \times 10^{23}\,\mathrm{cm}^{-2}$). Assuming that n_{H} is constant within the observed solid angle, it was fixed for the individual annuli. Since such an extremely high absorption especially affects the low energy domain, we restricted the observed energy range for each of the regions to $2.5 - 10$ keV. The results obtained from the fitting as well as the derived surface brightness are given in Table 4.3. According to the reduced χ^2 values of the regions, a power-law fit yields a very good estimation for each of the spectra.

Fig. 4.2 shows the spectrum of the second annulus. This plot contains some interesting implications of the analysis applied in this thesis. The two upper curves (dark blue and black) correspond to the pn data of the old and new observation since this instrument is more sensitive compared to the MOS cameras. Also clearly visible is the strong absorption below ≈ 3 keV. Obviously the two pn spectra match very well, yet the first energy bin of the dark blue data set (i.e. the data of the older observation) extends to higher energies. This effect arises from the significance binning. As the net exposure of the 2000 observation is well below the one of 2003, the energy bins must be broader in order to reach the requested significance (assuming a non-variable source). Of course the same argumentation is valid with reference to the MOS spectra.

The fitted spectral index of the annuli varies with angular distance to the pulsar, as shown in Fig. 4.3. From the first to the fourth annulus, it increases by roughly 0.7, reflecting a softening of the spectrum. In order to objectively test the hypothesis that the index increases with larger distance, a linear function was fitted to the data. The gradient and its error clearly exclude the possibility that the observed trend is just the result of a statistical fluctuation.

As can already be seen by a quick look at the *XMM-Newton* sky map, the surface brightness decreases with greater distance to CXOU J174722.8−280915. Fig. 4.4 confirms and quantifies this statement. The low statistical errors in this plot obviate the need for checking the slope as done for the index plot.

As illustrated in Fig. 4.5, the spectra were divided into several energy bins in which

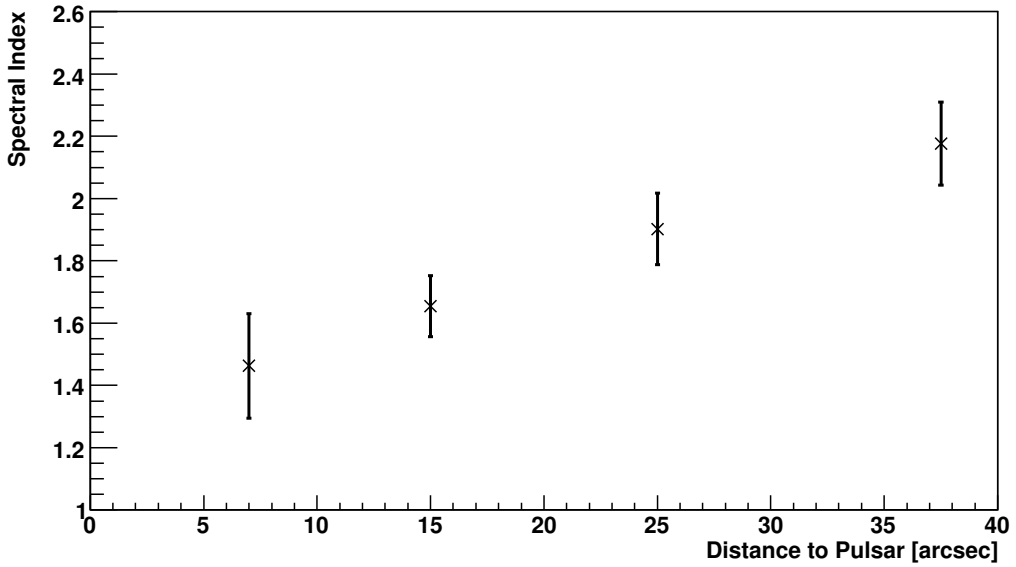

Fig. 4.3.: *Evolution of the fitted spectral index with increasing angular distance to the pulsar.*

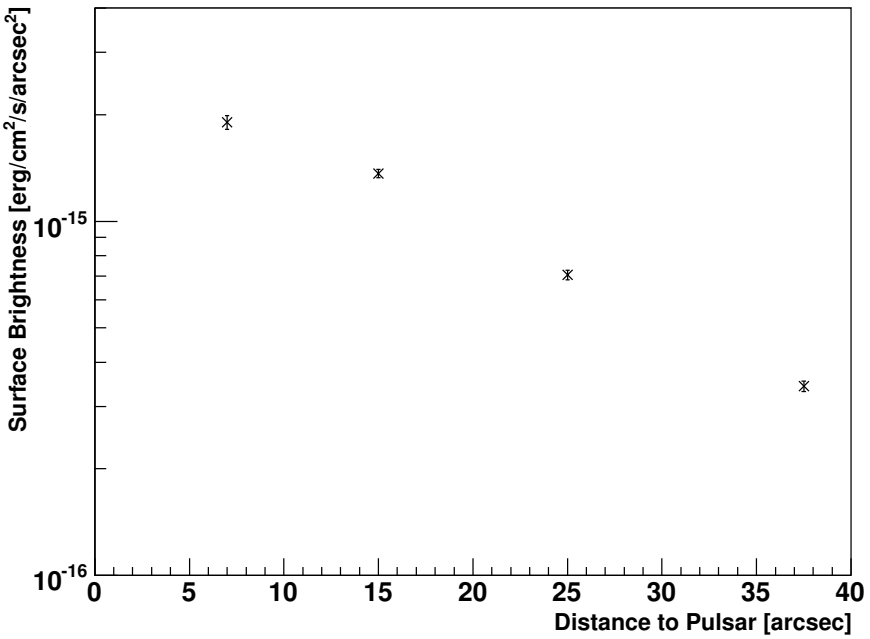

Fig. 4.4.: *Evolution of the surface brightness with increasing angular distance to the pulsar.*

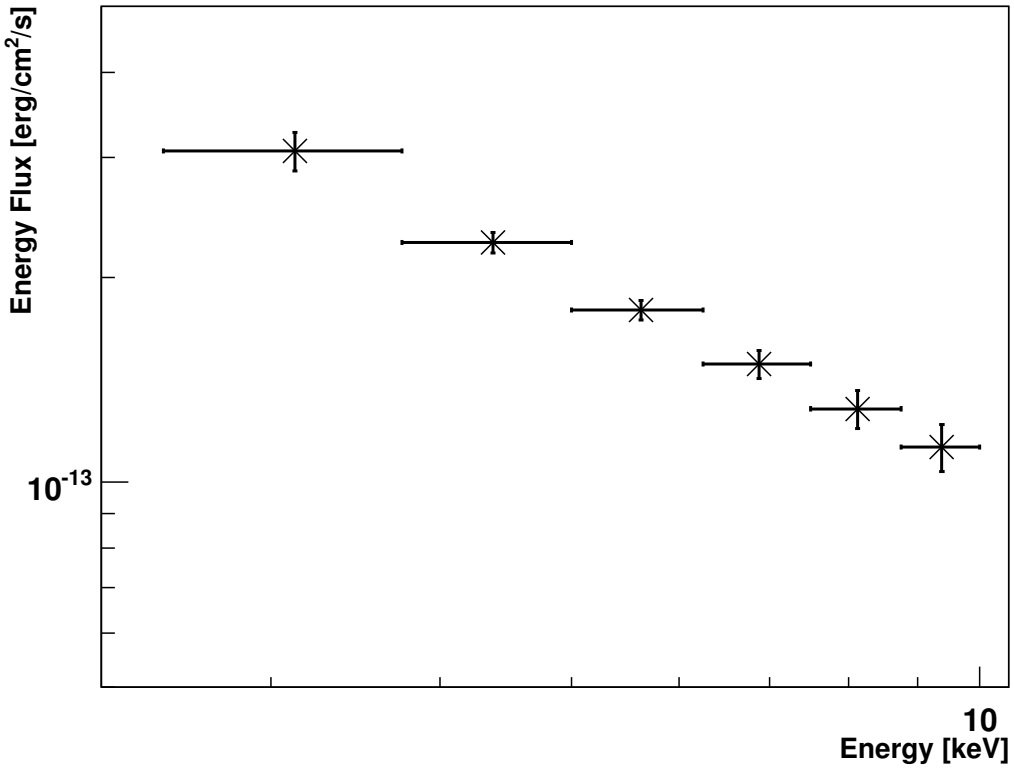

Fig. 4.5.: *Measured energy flux of the third annulus split into six bins of equal width between* 2.5 *and* 10 *keV. The abscissa ranges from* 2 *to* 10.5 *keV and the ordinate from* 5×10^{-14} *to* 5×10^{-13} *erg/cm*^{2}*/s, respectively.*

the unabsorbed flux was calculated. We chose six energy bins of equal width (1.25 keV) between 2.5 and 10 keV. This approach still contains all information necessary for the modeling and will be described in more detail in Section 5.5.1.

5. Modeling the Non-Thermal Emission of G0.9+0.1

In the following, the model applied to G0.9+0.1 is described in detail. Afterwards the results of the parameter optimization are presented and their implications for the VHE γ-ray emission discussed. This model has already been described and adopted to the PWN MSH 15−5*2* by Schöck et al. (2010). For a more comprehensive review, the reader is referred to the dissertation of F. M. Schöck (2010).

5.1. The Lepton Injection Spectrum

For a spatially resolved modeling as applied in this work, the first step is to estimate the energy distribution of the lepton population at the starting point of the modeling, i.e. at the wind termination shock. This distribution is going to be derived in the following.

5.1.1. General Remarks

A pulsar with spin-down-luminosity $\dot{E}$ emits part of its energy in the form of a particle wind, called the *pulsar wind* (see Section 2.1). As discussed, the particles constituting the pulsar wind are accelerated at the wind termination shock and injected into the PWN. The general shape of the injected lepton spectrum is commonly assumed to be a broken power law of the following form (e.g. Kennel & Coroniti 1984b; Reynolds & Chevalier 1984):

$$Q(E_\mathrm{e}, t) = \begin{cases} Q_0(t) \left(\dfrac{E_\mathrm{e}}{E_\mathrm{b}(t)} \right)^{-p_1} & \text{for} \quad E_\mathrm{e} < E_\mathrm{b}(t), \\ Q_0(t) \left(\dfrac{E_\mathrm{e}}{E_\mathrm{b}(t)} \right)^{-p_2} & \text{for} \quad E_\mathrm{e} \geq E_\mathrm{b}(t), \end{cases} \tag{5.1}$$

with the lepton energy E_e, the break energy $E_\mathrm{b}(t)$, the spectral indices Γ_1 and Γ_2 and the normalization $Q_0(t)$ of the spectrum. Since the model focuses on the inner part of the PWN close to the pulsar where mainly young leptons are expected to contribute to the non-thermal emission, we assume that the time scale of our modeling is small compared to the variability time scale of $E_\mathrm{b}(t)$ and $Q_0(t)$. Therefore the latter are considered constant, implying the same for $Q(E_\mathrm{e})$. Furthermore the applied model only aims to reproduce the measured X-ray and VHE γ-ray radiation, which allows to restrict the view to the part of the lepton spectrum where $E_\mathrm{e} \geq E_\mathrm{b}$. After applying the mentioned simplifications, the spectrum can be written as

$$Q(E_\mathrm{e}) = Q_0 \left(\frac{E_\mathrm{e}}{E_\mathrm{b}} \right)^{-p}, \tag{5.2}$$

where $p = p_2$ is the upper index of the broken power-law in Eq. 5.1. Defining $Q_0^{'} = Q_0 \, E_\mathrm{b}^p$ gives

$$Q(E_\mathrm{e}) = Q_0^{'} E_\mathrm{e}^{-p}, \tag{5.3}$$

which allows to work with a power-law-type lepton energy spectrum without explicitly inserting E_b[1]. When defining η as the conversion efficiency of the spin-down luminosity into the observed part of leptons, $Q_0^{'}$ can be derived as follows. The total amount of spin-down power transferred into lepton energy is given by

$$\int_{E_\mathrm{e,min}}^{E_\mathrm{e,max}} Q(E_\mathrm{e}) E_\mathrm{e}\,\mathrm{d}E_\mathrm{e} = \eta\dot{E}. \tag{5.4}$$

Inserting Eq. 5.3 then yields

$$Q_0^{'} \int_{E_\mathrm{e,min}}^{E_\mathrm{e,max}} E_\mathrm{e}^{-p+1}\,\mathrm{d}E_\mathrm{e} = \eta\dot{E}, \tag{5.5}$$

and integrated

$$Q_0^{'} = \begin{cases} \dfrac{\eta\dot{E}}{\ln\left(E_\mathrm{e,max}/E_\mathrm{e,min}\right)} & \text{for} \quad p = -2, \\ \dfrac{(2-p)\eta\dot{E}}{E_\mathrm{e,max}^{2-p} - E_\mathrm{e,min}^{2-p}} & \text{for} \quad p \neq -2. \end{cases} \tag{5.6}$$

In order to obtain a value for $Q_0^{'}$, the parameters have to be constrained. As mentioned in Section 2.3, $\dot{E}$ has been measured to 4.3×10^{37} erg/s for G0.9+0.1. The spectral index of the injection spectrum, p, can be derived by X-ray observations of emission close to the pulsar since it is related to the spectral index of the synchrotron radiation Γ by $p = 2\Gamma - 1$ (Eq. 2.12). Supposing that the leptons do not suffer strong synchrotron losses while propagating through the area which constitutes the first annulus of our *XMM-Newton* analysis (see Chapter 4), the spectral index of that annulus can be used to obtain p. The rounded value of $\Gamma = 1.5$ then implies $p = 2$. $E_\mathrm{e,min}$ and $E_\mathrm{e,max}$ will be discussed in Section 5.1.2 and 5.1.3, respectively. The conversion efficiency η remains as a free parameter of the optimization.

5.1.2. Minimum Lepton Energy

As explained above, for the purpose of the modeling applied in this work it is sufficient to simplify the broken power law (Eq. 5.1) to a single power law (Eq. 5.3). Then the simplest choice for $E_\mathrm{e,min}$ is certainly E_b, provided that an estimation for the latter is known. However, typical values for E_b are usually far too low to produce X-rays or VHE γ-rays. Therefore, increasing $E_\mathrm{e,min}$ might be useful since it significantly improves the computing efficiency.

The electron energy necessary to produce synchrotron photons of mean energy E_keV (in units of keV) in a magnetic field of strength $B = 10^{-5} B_{-5}\,\mathrm{G}$ is given by de Jager & Djannati-Ataï (2008) as

$$E_\mathrm{e} = (112\,\mathrm{erg}) B_{-5}^{-1/2} E_\mathrm{keV}^{1/2}. \tag{5.7}$$

The lowest energy relevant for the modeling is $E_\mathrm{keV} = 2.5$. The magnetic field strength was not known before the modeling. When adopting an extremely high field strength[2] of $B_{-5} = 10$ (corresponding to $B = 100\,\mu\mathrm{G}$), the required electron energy becomes $E_\mathrm{e} =$

[1] This holds as long as there is no doubt that the observed energy range lies above E_b.
[2] This, however, is not expected for G0.9+0.1, as mentioned in Section 2.2.

56 erg. A similar expression for the mean electron energy required to scatter CMB photons up to an energy E_{TeV} is given by (de Jager & Djannati-Ataï 2008):

$$E_{\mathrm{e}} = (29\,\mathrm{erg}) E_{\mathrm{TeV}}^{1/2}. \tag{5.8}$$

The VHE modeling presented in this work starts at an energy of 0.2 TeV, resulting in $E_{\mathrm{e}} = 13\,\mathrm{erg}$. For G0.9+0.1, we chose $E_{\mathrm{e,min}} = 1\,\mathrm{erg}$, considerably lower than both of the values stated in this Section. Furthermore, before performing the parameter optimization, we carefully checked if an even lower value of $E_{\mathrm{e,min}}$ has any influence on the results, which is not the case.

5.1.3. Maximum Lepton Energy

Independent of the acceleration mechanism, there are two limits which constrain the maximum energy a lepton can be accelerated to at the termination shock. These two constraints are presented in the subsequent paragraphs.

Gyroradius Limit At low energies, the leptons are confined within the shock due to the magnetic field. Because of the acceleration, however, the gyroradius (also called Larmor radius) of a particle gets enlarged further and further until it is comparable to the radius of the termination shock[3], and thus the lepton is no longer confined within the shock. This gyroradius limit was first formulated by Harding & Gaisser (1990). The following derivation conforms to the one of Schöck (2010). The Larmor radius is given by

$$r_{\mathrm{L}} = \frac{E_{\mathrm{e,max}}}{eB_{\mathrm{S}}}, \tag{5.9}$$

with B_{S} denoting the magnetic field strength at the termination shock. Requiring

$$r_{\mathrm{L}} = \epsilon R_{\mathrm{S}}, \tag{5.10}$$

where $0 < \epsilon < 1$, one obtains

$$E_{\mathrm{e,max}} = \epsilon e R_{\mathrm{S}} B_{\mathrm{S}}. \tag{5.11}$$

Inserting the expression for the shock magnetic field strength from Kennel & Coroniti (1984b), the limit can be written as

$$E_{\mathrm{e,max}} = \epsilon e \kappa \sqrt{\frac{\sigma}{1+\sigma}\frac{\dot{E}}{c}}, \tag{5.12}$$

where κ denotes the magnetic compression ratio at the shock and σ the magnetization parameter. The gyroradius limit mainly becomes relevant for PWNe with low magnetic fields. An estimation of ϵ for a Vela-like pulsar was derived by de Jager & Djannati-Ataï (2008). In case of a maximum energy of 350 TeV, ϵ would then be equal to 0.2. Due to the lack of other estimations, that parameter was fixed to the same value for the scenarios *(a)* and *(b)* in this work (see Section 5.6). For *Scenario (c)*, ϵ was left unconstrained, except for the foresaid condition that $0 < \epsilon < 1$.

[3]Note that this is only possible when the synchrotron limit is not reached yet (see next paragraph)

Synchrotron Limit The second limit to be taken into account was first introduced by de Jager et al. (1996). These authors discuss that a particle moving through a magnetic field reaches its maximum energy when the synchrotron losses become as strong as the energy gain. Following the nomenclature of Schöck (2010), the time derivative of the lepton energy is then

$$\frac{\mathrm{d}E_e}{\mathrm{d}t} = \frac{\alpha e c B_\mathrm{S}}{2\pi} - \frac{2e^4 B_\mathrm{S}^2 \gamma^2 \sin^2\theta}{3 m_\mathrm{e} 2 c^3}, \tag{5.13}$$

where θ denotes the pitch angle between the magnetic field and the particle's direction of motion. $\alpha \leq 1$ is a constant depending on the shock geometry. The first term in this equation expresses the energy gain of a lepton through first order Fermi acceleration, whereas the second one corresponds to the synchrotron losses of that particle. de Jager et al. (1996) then obtain the maximum lepton energy by setting $\mathrm{d}E_e/\mathrm{d}t = 0$ and solving

$$E_\mathrm{e,max} = \gamma_\mathrm{max} m_\mathrm{e} c^2 = 1.9 \times 10^{13} \left(\frac{\alpha}{\langle \sin^2\theta \rangle B_\mathrm{S,G}} \right) \mathrm{eV}, \tag{5.14}$$

with $B_\mathrm{S,G}$ the magnetic field strength in units of G. Setting $\alpha = 1$, inserting $\langle \sin^2\theta \rangle = 1/2$ and converting to erg, Eq. 5.14 becomes

$$E_\mathrm{e,max} = 43.7\, B_\mathrm{S,G}^{-1/2}\, \mathrm{erg}. \tag{5.15}$$

For given parameters (referring to ϵ, κ, σ and R_S) it is now possible to derive the synchrotron and gyroradius limits. The lower one of these values is then used as $E_\mathrm{e,max}$.

5.2. Outward Propagation of the Leptons

As described in the preceding Sections, the injection lepton spectrum responsible for the X-rays and VHE γ-rays can be approximated by a single power law in a certain energy range. These leptons then propagate downstream beyond the termination shock.

The adopted velocity profile resembles the one from Schöck (2010),

$$v(r) = v_\mathrm{S} \left(\frac{R_\mathrm{S}}{r} \right)^\alpha, \tag{5.16}$$

with α the index of the power law and v_S the velocity at the wind termination shock. The index is kept free for the parameter optimization. The shock velocity v_S was determined to be $c/3$ for the Crab Nebula by Kennel & Coroniti (1984a). This value was also used by Schöck (2010) for modeling MSH 15−5*2*. However, determing v_S in the case of G0.9+0.1 is very complicated. As mentioned in Section 2.2, Porquet et al. (2003) read the observed east-west gradient in the spectral index as an evidence for fast rotation with resulting Doppler boosting of the leptons in the PWN, which would strongly exacerbate the situation for that source. But, as stated in the same Section, the observations performed in the radio regime by Dubner et al. (2008) do not support any spectral east-west variations. For want of better estimates, we therefore also set the shock velocity to $c/3$.

The applied model assumes spherical symmetry, leading to a merely radial outward propagation of the leptons. As is clearly visible by looking at Fig. 4.1, the appearance of

G0.9+0.1 in X-rays deviates from radial symmetry. Nevertheless, such a model is definitely an improvement compared to one-zone models which attempt to reproduce the radiation of a PWN using a single, localized lepton population.

Another important physical quantity is the strength of the magnetic field at the shock, B_{S}. A relation for this is given by Kennel & Coroniti (1984a) and Sefako & de Jager (2003):

$$B_{\mathrm{S}} = \frac{\kappa}{R_{\mathrm{S}}} \sqrt{\frac{\sigma}{1+\sigma} \frac{\dot{E}}{c}} \,. \tag{5.17}$$

For the modeling applied in this work, it is useful to combine the compression ratio κ and the magnetization parameter σ by defining a new parameter

$$\xi = \kappa \sqrt{\frac{\sigma}{1+\sigma}} \,. \tag{5.18}$$

Eq. 5.17 then becomes

$$B_{\mathrm{S}} = \frac{\xi}{R_{\mathrm{S}}} \sqrt{\frac{\dot{E}}{c}} \,. \tag{5.19}$$

Assuming a toroidal magnetic field whose outward propagation is strongly connected to that of the leptons, the ideal magnetohydrodynamic limit yields (Schöck 2010)

$$\frac{\partial \vec{B}}{\partial t} = \nabla \times \left(\vec{v} \times \vec{B} \right) . \tag{5.20}$$

As already discussed in Section 5.1, the model focuses on reproducing the inner part of the PWN, leading to the simplification of a static system. In that case, the time-dependence of Eq. 5.20 disappears, leading to

$$0 = \nabla \times \left(\vec{v} \times \vec{B} \right) . \tag{5.21}$$

Using this simplification, Kennel & Coroniti (1984a) derived the following relation, assuming a toroidal magnetic field:

$$Bvr = B_{\mathrm{S}} v_{\mathrm{S}} R_{\mathrm{S}} = \text{const.} \tag{5.22}$$

This can be rewritten to

$$B = \frac{B_{\mathrm{S}} v_{\mathrm{S}} R_{\mathrm{S}}}{vr} . \tag{5.23}$$

When inserting Eq. 5.16, the magnetic field becomes a function of only one variable, r:

$$B = B_{\mathrm{S}} \left(\frac{R_{\mathrm{S}}}{r} \right)^{1-\alpha} . \tag{5.24}$$

For given parameters α, R_{S} and ξ it is now possible to calculate the bulk velocity and magnetic field strength at a given point in the PWN. The next step is to look at the development of the lepton population.

As the leptons propagate outwards, they suffer energy losses, leading to a change of the spectral shape. According to de Jager & Harding (1992), two fundamental energy loss mechanisms have to be considered:

$$\frac{\mathrm{d}E_{\mathrm{e}}}{\mathrm{d}t} = -\frac{E_{\mathrm{e}}}{3} \nabla \cdot \vec{v}_{\perp} + \dot{E}_{\mathrm{e,rad}} . \tag{5.25}$$

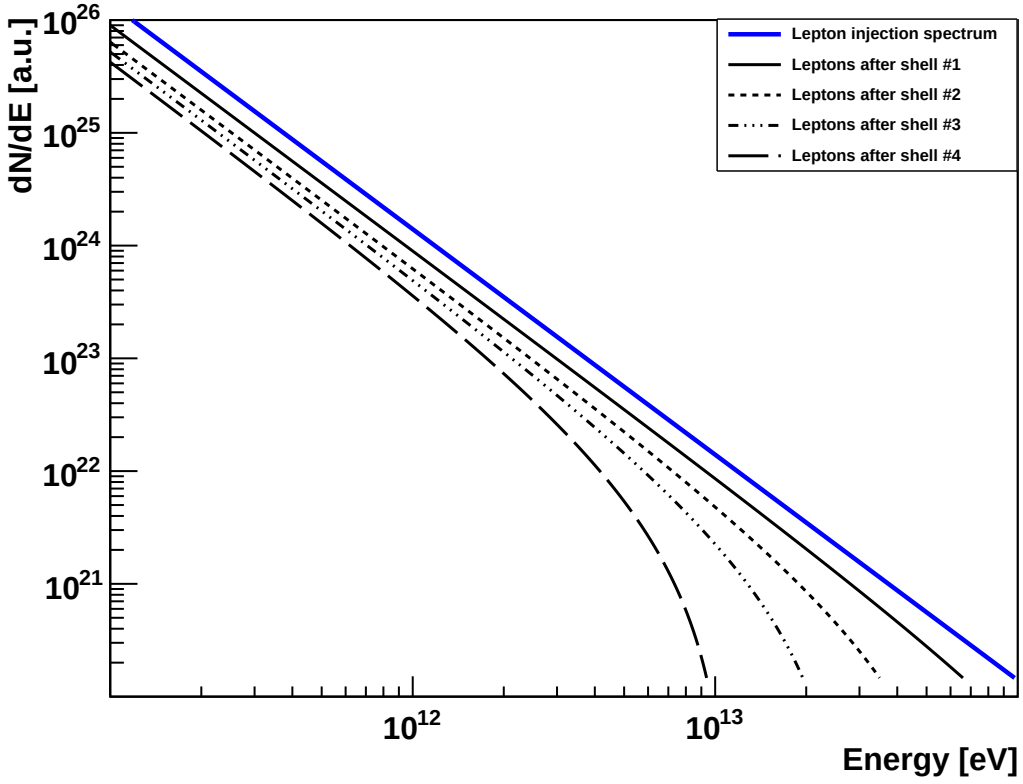

Fig. 5.1.: *Development of a power-law lepton injection spectrum for a population that propagates outwards and undergoes adiabatic and synchrotron energy losses. The uncooled spectrum (blue) has a spectral index of 2 and is defined between* 10^{11} *and* 10^{14} *eV. The magnetic field strength was set constant to* $50\,\mu G$.

The first term corresponds to adiabatic or expansion losses of the leptons. $\vec{v}_\perp$ refers to the radial component of the outflow velocity. Since our model assumes a strictly radial propagation, this term can be rewritten to

$$\left(\frac{\mathrm{d}E_\mathrm{e}}{\mathrm{d}t}\right)_\mathrm{Ad} = -\frac{E_\mathrm{e} v_\mathrm{S}}{3R_\mathrm{S}}\,(2-\alpha)\,\left(\frac{R_\mathrm{S}}{r}\right)^{\alpha+1}. \tag{5.26}$$

The second term of Eq. 5.25 denotes the energy change of the leptons due to radiation losses. In the case of G0.9+0.1, the synchrotron losses are supposed to surpass the IC losses by far and therefore the latter are neglected. The radiation losses are then given by (de Jager & Harding 1992; Schöck 2010)

$$\left(\frac{\mathrm{d}E_\mathrm{e}}{\mathrm{d}t}\right)_\mathrm{Sy} = -2.368\times10^{-3}(BE_\mathrm{e})^2\,\frac{\mathrm{erg}}{\mathrm{s}}. \tag{5.27}$$

Fig. 5.1 shows the development of a power-law lepton energy spectrum of a population that propagates outwards and suffers from adiabatic and synchrotron losses. The adiabatic losses (see Eq. 5.26) are proportional to the lepton energy, which means that they do not change the shape of the spectrum, but just "shift" it to lower energies. The synchroton losses, however, depend on the square of the lepton energy. This especially affects the higher energies, leading to a cutoff in the spectrum.

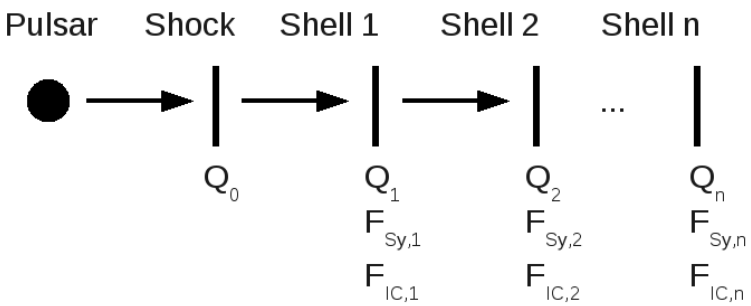

Fig. 5.2.: *Scheme illustrating the shells used for the modeling. The lepton population injected at the termination shock is propagated outwards shell by shell. At each shell, the synchrotron and IC radiation as well as the energy losses of the leptons are calculated. Image taken from Schöck (2010).*

5.3. Numerical Implementation

In order to be able to numerically implement the model that was laid out in the previous Sections, the observed part of the PWN was divided into a number of shells, as is illustrated in Fig. 5.2. This is a valid approach as long as the shell number n is chosen high enough. Depending on the required precision, we chose a shell number between several hundreds and up to 1000 (for a more detailed review on the precision see Section 5.5).

At first, the lepton injection spectrum is calculated for the given parameters, as described in Section 5.1. Using the energy losses described in Section 5.2, the lepton spectrum can then be propagated outwards shell by shell. At this step, it is important to note that this lepton spectrum is actually a lepton rate, as can be seen by e.g. looking at Eq. 5.6. However, when calculating the photon emission of a shell, the lepton spectrum is required. Therefore one has to multiply the rate with the time the leptons stay in the considered shell:

$$\left.\frac{\mathrm{d}N(E_\mathrm{e})}{\mathrm{d}E}\right|_j = Q_j(E_\mathrm{e})\,\Delta t_j. \tag{5.28}$$

For each shell, the emitted synchrotron and IC radiation can then be calculated as discussed in Section 2.1.2.

5.4. From 3D Shells to 2D Annuli

In the preceding Sections, the applied radially symmetric model has been described in detail. By dividing the PWN into a large number of shells and calculating the synchrotron and IC emission, the non-thermal radiation can be reproduced for a certain parameter set. However, since the model is three-dimensional, a shell (or the ensemble of several adjacent shells) actually corresponds to a hollow sphere. An annulus, as chosen for the X-ray analysis, is therefore merely the two-dimensional projection of the three-dimensional shells. This has two essential effects:

(a) Only part of the volume of a shell is visible in the projection represented by an annulus.

(b) Outer shells add up to an annulus' emission.

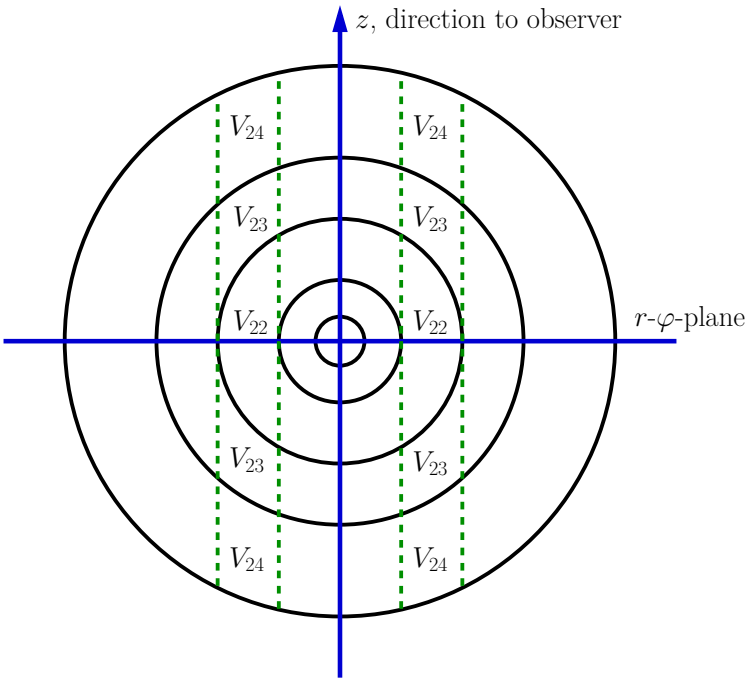

Fig. 5.3.: *Sketch illustrating the projection effect. As an example, a superposition of parts of the second, third and fourth shell contributes to the emission of the second annulus.*

In the following the conversion from 3D hollow spheres to 2D annuli is being derived. Assuming low angular source extension, as is clearly the case for G0.9+0.1, it is possible to use cylindrical coordinates. The whole volume of the shell j can easily be calculated as

$$V_j = \frac{4\pi}{3}\left(R_{\mathrm{out},j}^3 - R_{\mathrm{in},j}^3\right), \tag{5.29}$$

where $R_{\mathrm{in},j}$ and $R_{\mathrm{out},j}$ are the inner and outer radius of that shell, respectively. The differential volume element in cylindrical coordinates is given by

$$\mathrm{d}V = r\,\mathrm{d}r\,\mathrm{d}\varphi\,\mathrm{d}z. \tag{5.30}$$

For the following derivations, the point of origin is set to the center of the PWN. The z axis is represented by the line of sight. In case of a hollow sphere, the angle extends to all values of a full circle, $\varphi \in [0, 2\pi[$. The radius lies between the inner and the outer radius of the corresponding shell, $r \in [R_{\mathrm{in}}, R_{\mathrm{out}}[$. The z coordinate is a function of r and has to fulfill the following condition:

$$z^2 \leq R_{\mathrm{out}}^2 - r^2. \tag{5.31}$$

The first quantity to be derived is the part of the volume of shell i which lies in the line of sight of annulus i,

$$V_{ii} = \int \mathrm{d}V = \int_0^{2\pi} \mathrm{d}\varphi \int_{R_{\mathrm{in},i}}^{R_{\mathrm{out},i}} r\,\mathrm{d}r \int_{-\sqrt{R_{\mathrm{out},i}^2 - r^2}}^{\sqrt{R_{\mathrm{out},i}^2 - r^2}} \mathrm{d}z = \tag{5.32}$$

$$= 4\pi \int_{R_{\mathrm{in},i}}^{R_{\mathrm{out},i}} r\sqrt{R_{\mathrm{out},i}^2 - r^2}\,\mathrm{d}r.$$

This integral can be solved analytically and yields

$$V_{ii} = \frac{4\pi}{3}\left(R_{\mathrm{out},i}^2 - R_{\mathrm{in},i}^2\right)^{3/2}. \tag{5.33}$$

Secondly, the contribution of shell j to annulus i (only relevant for $j > i$, counting from inner to outer shells) is required. Taking care to insert the right upper and lower integration boundaries, the calculation ensues similarly:

$$V_{ij} = 2\int_0^{2\pi} \mathrm{d}\varphi \int_{R_{\mathrm{in},i}}^{R_{\mathrm{out},i}} r\,\mathrm{d}r \int_{\sqrt{R_{\mathrm{out},j-1}^2 - r^2}}^{\sqrt{R_{\mathrm{out},j}^2 - r^2}} \mathrm{d}z = \tag{5.34}$$

$$= \frac{4\pi}{3}\left(\left[R_{\mathrm{out},j}^2 - R_{\mathrm{in},i}^2\right]^{3/2} - \left[R_{\mathrm{out},j}^2 - R_{\mathrm{out},i}^2\right]^{3/2}\right) + \frac{4\pi}{3}\left(\left[R_{\mathrm{out},j-1}^2 - R_{\mathrm{out},i}^2\right]^{3/2} - \left[R_{\mathrm{out},j-1}^2 - R_{\mathrm{in},i}^2\right]^{3/2}\right).$$

Given the assumption that the radiation is emitted isotropically and does not undergo any absorption inside the PWN, the resulting spectrum of annulus i is

$$\left.\frac{\mathrm{d}N}{\mathrm{d}E}\right|_{i,\mathrm{res}} = \sum_{j\geq i} \frac{V_{ij}}{V_j} \left.\frac{\mathrm{d}N}{\mathrm{d}E}\right|_j \tag{5.35}$$

with $\mathrm{d}N/\mathrm{d}E|_j$ the spectrum of shell j. The ratio $\dfrac{V_{ij}}{V_j}$ can also be written as a tensor v_{ij} with all entries equal to zero for $j < i$. Eq. 5.35 then becomes

$$\left.\frac{\mathrm{d}N}{\mathrm{d}E}\right|_{i,\mathrm{res}} = \sum_{j} v_{ij} \left.\frac{\mathrm{d}N}{\mathrm{d}E}\right|_j. \tag{5.36}$$

The entries of v_{ij} can be written in a matrix of size $n \times n$. For the chosen extraction regions of G0.9+0.1, n equals 4, and one obtains with the chosen radii (see Table 4.2):

$$v = \begin{pmatrix} 0.82 & 0.22 & 0.07 & 0.03 \\ 0 & 0.74 & 0.33 & 0.12 \\ 0 & 0 & 0.59 & 0.26 \\ 0 & 0 & 0 & 0.59 \end{pmatrix}. \tag{5.37}$$

This means that, for example, a superposition of 74 % of the second, 33 % of the third and 12 % of the fourth shell contributes to the emission of the second annulus. The composition of that annulus is also illustrated in Fig. 5.3.

5.5. Parameter Optimization

With the model described in the preceding Sections it is possible to calculate the emission of an annulus for given parameters R_{S}, η, ξ, α and ϵ. In the following, it will be shown how to compare this modeled with the measured data. Afterwards the influence of the numerical precision on the quality of the modeled data is examined and the possible parameter ranges are discussed.

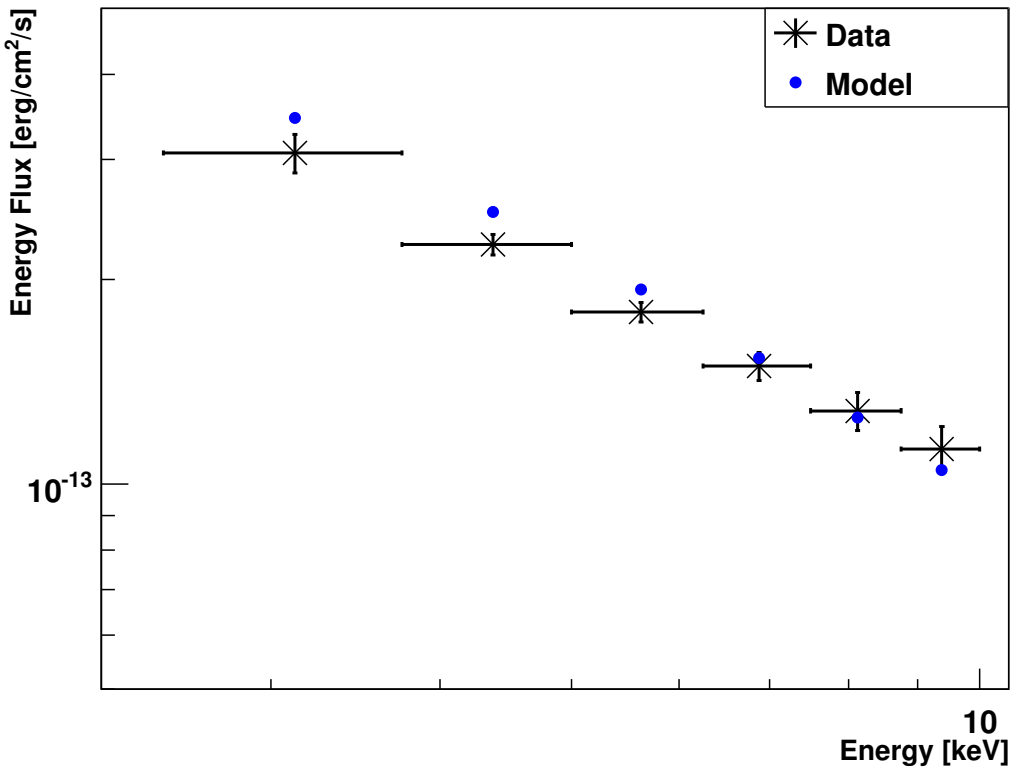

Fig. 5.4.: *Energy flux split into several bins: measured data of the third annulus including the statistical errors (black) and the modeled energy flux for Scenario (b) (see description in Section 5.6). The abscissa ranges from 2 to 10.5 keV and the ordinate from* 5×10^{-14} *to* 5×10^{-13} *erg/cm*^{2}*/s, respectively.*

5.5.1. Comparison of Measured and Modeled Data

As briefly mentioned in Section 4.4, we calculated the measured energy flux in six energy bins between 2.5 and 10 keV for each of the four annuli. These results can be compared with the ones obtained from the modeling by calculating the χ^2 value:

$$\chi^2 = \sum_i \left(\frac{F_{i,\mathrm{XMM}} - F_{i,\mathrm{mod}}}{\Delta F_{i,\mathrm{XMM}}} \right)^2 , \tag{5.38}$$

where $F_{i,\mathrm{XMM}}$ and $F_{i,\mathrm{mod}}$ denote the measured and modeled flux and $\Delta F_{i,\mathrm{XMM}}$ the statistical error in the corresponding energy bin. Fig. 5.4 shows as an example the measured energy flux points for the third annulus as well as the best-matched model points for *Scenario (b)* (further information on the scenarios and results in the following Section). By dividing the spectra of the four annuli into the energy bins and calculating the χ^2 value it is possible to optimize the parameters by taking into account the overall energy flux as well as the spectral shape. Another possibility would have been to calculate χ^2 using the undivided energy flux of the annuli and their spectral indices. Then, however, it would have been necessary to fit the modeled spectra before calculating the χ^2. Apart from requiring more computational resources, this latter approach is also disfavored because one has to assume a spectral shape for the modeled data in that case, which is not necessary

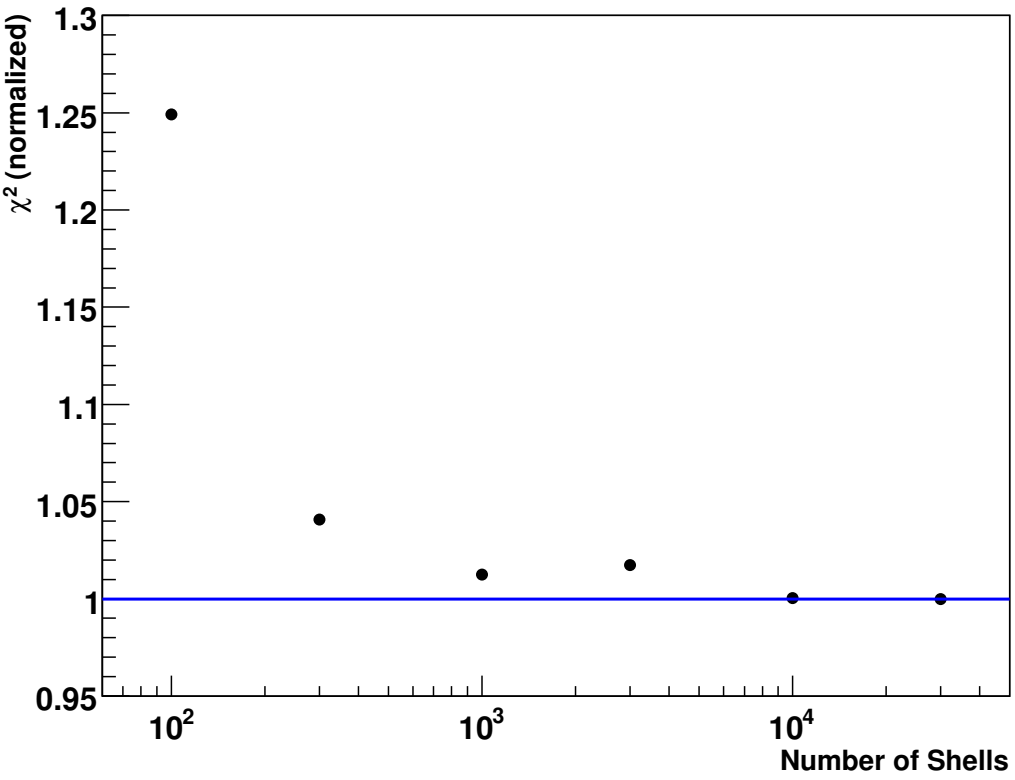

Fig. 5.5.: *Dependence of the χ^2 value on the shell number for the optimized parameter set of Scenario (b) (see Table 5.1). χ^2 was normalized to the value obtained for a shell number of $n = 30\,000$ (represented by the blue line).*

in our method.

5.5.2. Calculation Precision and Constraints on the Parameters

As described in Section 5.3, the PWN was divided into a number of shells n in order to be able to numerically calculate the modeled emission. On the one hand, the number of shells should be large enough to keep the numerical precision, which is more strongly affected by discretization errors for small values of n, sufficiently high. On the other hand, a higher shell number also implies a longer computing time.

The dependence of the χ^2 value on the shell number n was examined. The results are plotted in Fig. 5.5 and normalized to the one obtained for $n = 30\,000$. While the result for $n = 100$ still strongly deviates from this reference value, the calculations for $n = 300$ and $n = 1000$ are already quite satisfactory, depending on the required precision.

The second parameter that strongly influences the precision of the model as well as the computing efficiency is the step width chosen for the numerical integration in Eq. 2.7. Similar to the dependence on the shell number, Fig. 5.6 illustrates the achieved numerical quality of the model when varying the integration precision for the synchrotron emission. The values given on the X-axis correspond to the number of steps chosen for the numerical integration, i.e. the inverse of the integration precision.

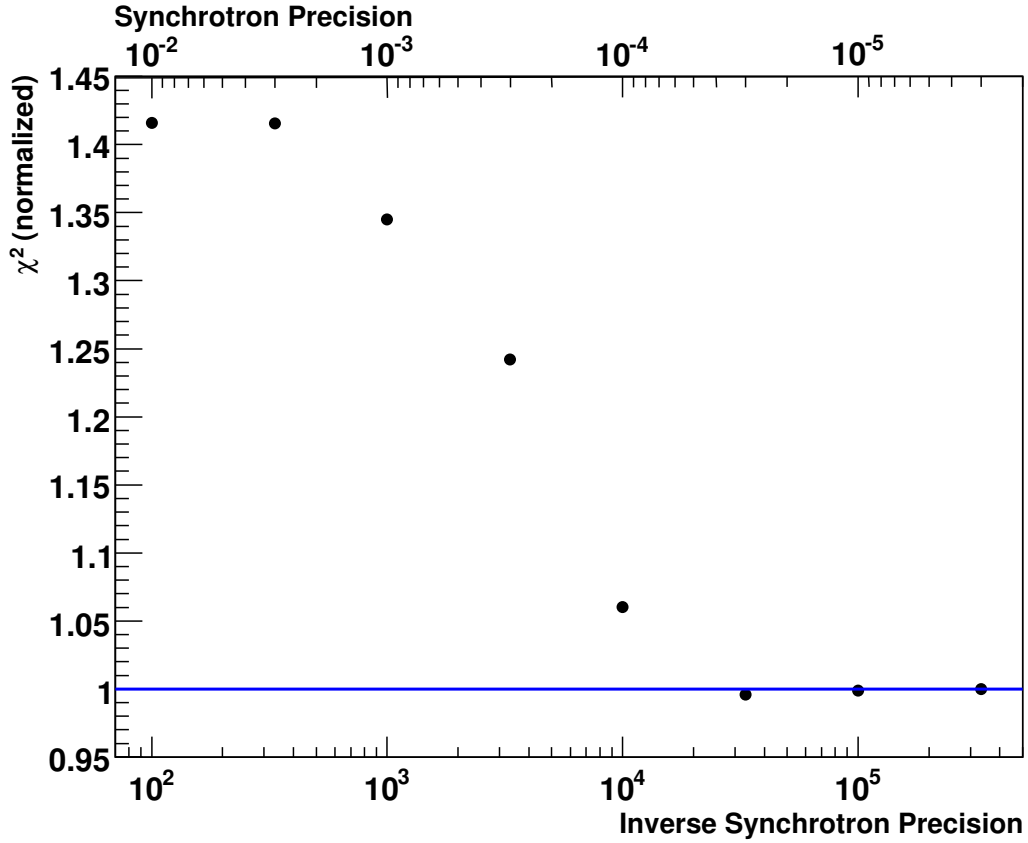

Fig. 5.6.: *Dependence of the χ^2 value on the synchrotron precision for the same parameter set as used for Fig. 5.5. χ^2 was normalized to the value reached for the highest precision (blue line). Note that the values on the lower abscissa denote the inverse synchrotron precision, corresponding to the number of steps used for the numerical integration. The additional upper abscissa gives the corresponding actual synchrotron precision.*

The next issues to discuss are the parameters of the model and their possible values. The first free parameter necessary for the calculation of the lepton injection spectrum is the conversion efficiency η. Since it is equal to the percentage of the pulsar's spin-down luminosity converted into the energy of the modeled leptons, it can in principle assume any value between 0 and 1. The combined parameter ξ was already defined as $\xi = \kappa\sqrt{\sigma/(1+\sigma)}$ in Eq. 5.18. The compression ratio κ usually lies in the range $1-3$ (Kennel & Coroniti 1984b). As mentioned in Section 2.1, the outflow beyond the termination shock is supposed to be particle-dominated, implying $\sigma < 1$. Taking both constraints into account, the possible values for ξ range between 0 and 2.5. Another free parameter is α, the index of the velocity function in Eq. 5.16. It was constrained to $\alpha > 0$, since a negative value would correspond to an acceleration downstream beyond the termination shock, which is definitely not expected. Furthermore, $\alpha > 2$ was also excluded in this work because that would result in an adiabatic energy gain of the leptons (see Eq. 5.26). The ratio between the gyroradius and the radius of the termination shock, ϵ, was already introduced and discussed in Section 5.1.3. It was fixed to a value of $\epsilon = 0.2$ for *Scenarios (a)* and *(b)* and kept free in the range $0 < \epsilon < 1$ for *Scenario (c)* (see next Section). The last remaining parameter is the extent of the termination shock R_{S}. As described in Section 2.2, Gaensler

et al. (2001) propose an extremely large value of R_S for G0.9+0.1. We consider this as rather unlikely and therefore did not follow this interpretation. Instead we assumed that R_S is much smaller and could not be resolved in the *Chandra* data set due to a too low exposure. The only constraint on R_S used in this work is a maximum value of 4 arcseconds for the angular extent of the shock radius, corresponding to the inner radius of the first annulus of the *XMM-Newton* analysis.

Since some of the parameters show a strong correlation, no conventional fitting routine was used. Instead they were scanned over the possible range, and for each parameter set the χ^2 was calculated. For the first scan, the whole possible range was used for every parameter. Despite choosing a rather large step width, this scan encompassed several ten thousand parameter sets. However, since the required model precision is not very high yet, a shell number of 300 and an inverse synchrotron precision of 5 000 steps per numerical integration were sufficient. When further constraining the parameters, a more accurate calculation is necessary. For this refined scan, we used an amount of 1 000 shells and an inverse synchrotron precision of 20 000 for each parameter set.

5.6. Results of the Modeling

It was already laid out in Section 2.3 that the distance to G0.9+0.1 is not well constrained. While many authors suppose that the system is located in the vicinity of the GC, implying $d \approx 8.5\,\mathrm{kpc}$, newer measurements point to a considerably larger distance of $\approx 13\,\mathrm{kpc}$. Since no argument in favor of either scenario was known, we treated both on an equal footing and carried out the parameter optimization separately for both of them. This was easily implemented since the unfixed parameter R_S was actually varied by changing its angular extent φ_S. For small angles, they are both proportionally related by

$$R_S = d_{\mathrm{pc}}\,\varphi_S \cdot \mathrm{AU}, \tag{5.39}$$

with d_{pc} the assumed distance in units of pc, and AU one astronomical unit. By using this definition, φ_S needs to be expressed in units of arcseconds.

The radial dependence of the spectral index and surface brightness obtained by analyzing the *XMM-Newton* data was already shown and discussed in Section 4.4. One of the major objectives of the applied model is to reproduce the evolution of these two values. After having carried out the parameter optimization, the best-fit results can be further investigated by comparing the properties of the modeled data with the measured ones. The measured and optimized modeled values of the spectral index for *Scenario (a)*, assuming a distance of 8.5 kpc and with ϵ fixed to a value of 0.2, are presented in Fig. 5.7. Although the modeled index also increases with growing distance to the pulsar, the shape is obviously too flat. In Fig. 5.8 the measured values of the surface brightness are plotted together with the ones obtained from the modeling of the same scenario. As can be seen, the results obtained from the parameter optimization agree very well with the measured data.

The next issues to be discussed are the results of the independent parameter optimization for *Scenario (b)* where the distance is assumed to be 13 kpc and ϵ is again fixed to 0.2. The results for this scenario are shown in Fig. 5.9. Surprisingly, the plots are hardly distinguishable from the ones of the first scenario. In order to better understand this peculiarity, the calculated best parameters for both scenarios are shown in Table 5.1 and will be discussed in the following. In both cases, the angular extent of the termination shock, φ_S, equals its upper limit of 4 arcseconds. Converted into the spatial extent this

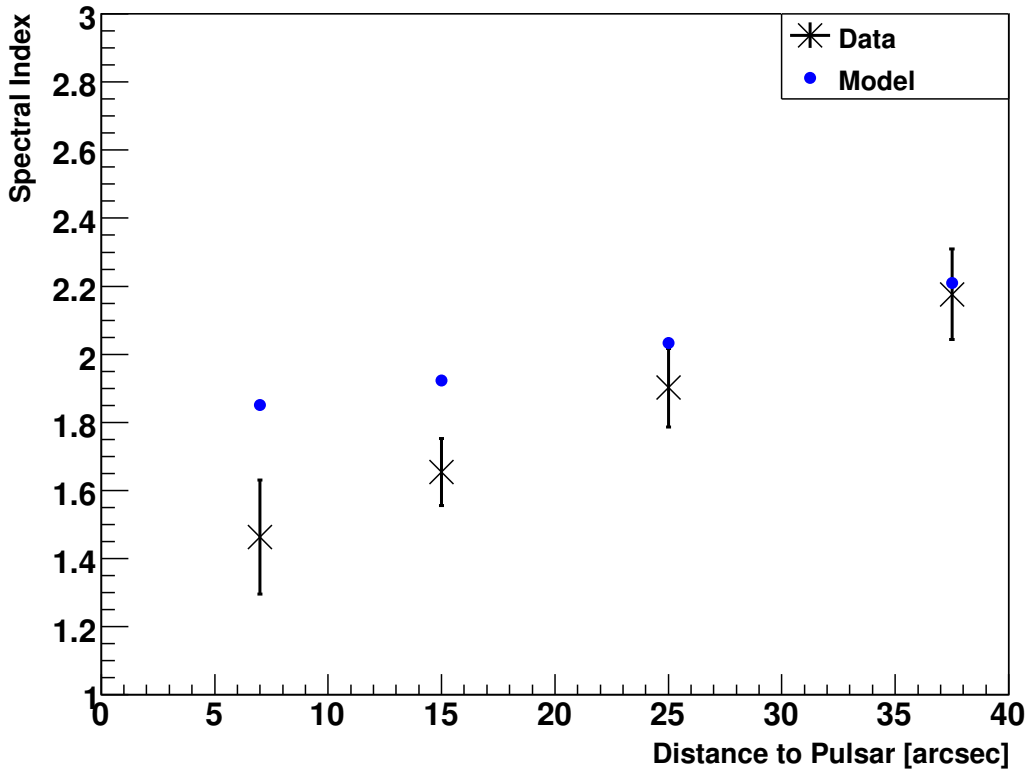

Fig. 5.7.: *Comparison of the measured and optimized modeled spectral index of the annuli for Scenario (a).*

Table 5.1.: *Best-fit results of the parameters as well as the shock radius and magnetic field for Scenario (a) (8.5 kpc) and Scenario (b) (13 kpc).*

Parameter	8.5 kpc	13 kpc
η	0.15	0.36
ξ	0.12	0.14
α	1.27	1.27
φ_S [arcsec]	4.0	4.0
R_S [pc]	0.16	0.25
B_S [μG]	8.79	6.57

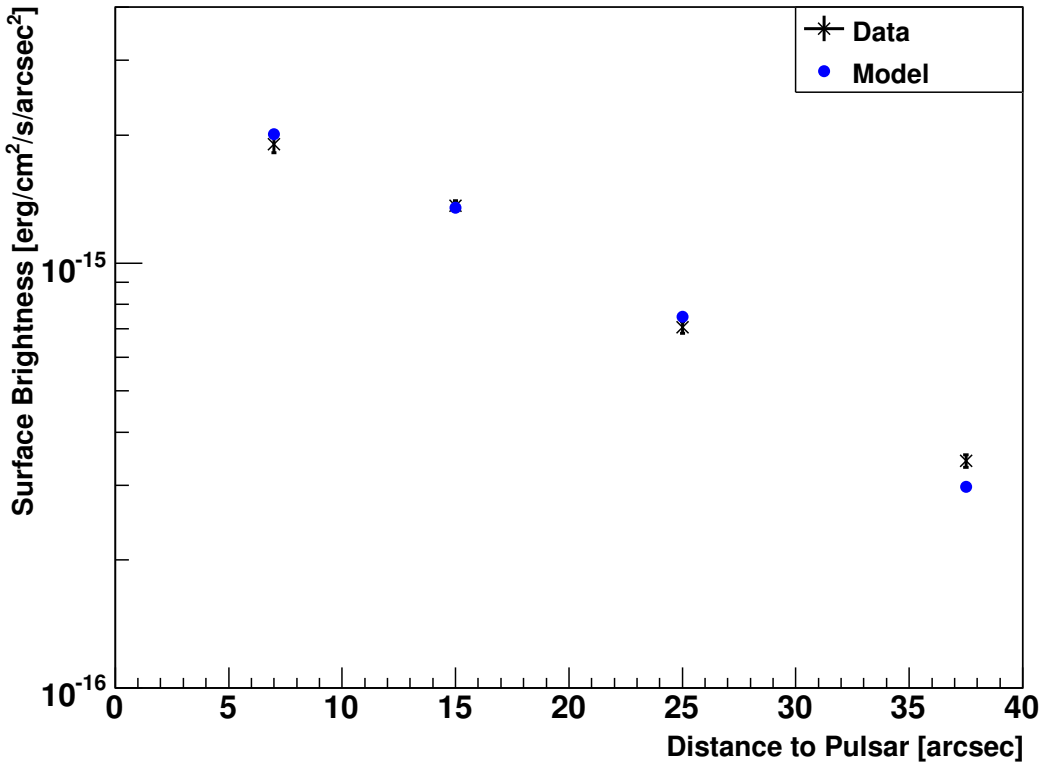

Fig. 5.8.: *Measured and modeled best-fit surface brightness for Scenario (a), which assumes a distance of* 8.5 *kpc.*

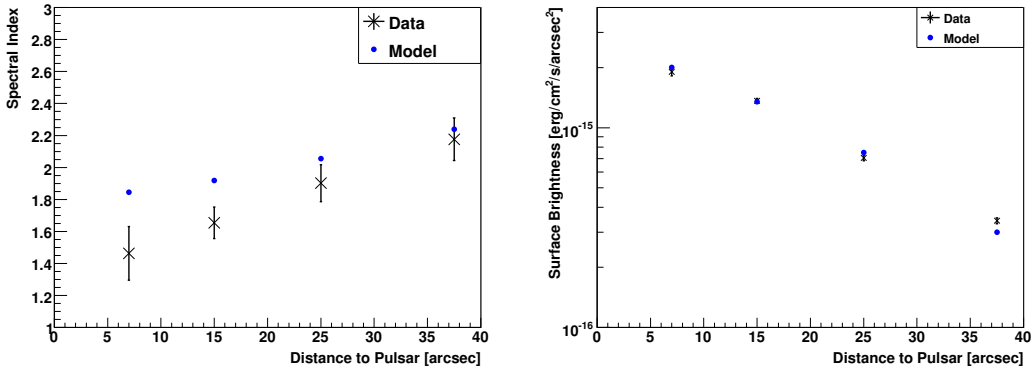

Fig. 5.9.: *Left: Measured and modeled index of the best-fit parameter set for Scenario (b). Right: Comparison of measured and modeled surface brightness for the same parameters.*

results in an increased shock radius for the high-distance scenario. The velocity profile is determined by its index α. The best-fit result of this value is also identical for both scenarios. Identical values of φ_S and α imply that, literally spoken, the parameter scan tends to select the same image of a PWN for different distances. This, however, has two implications for the remaining parameters. Firstly, the conversion efficiency η has to be different for both scenarios because the overall X-ray luminosity of the PWN is increased for larger distances. This means that η needs to be higher for such a scenario. Secondly, the magnetic field strength has to be increased for a lower distance in order to achieve the same spectral steepening for the smaller PWN.

For both scenarios the modeled spectral index of the first annulus lies well above the measured one. At first this seems quite puzzling because the index of the lepton spectrum was chosen such that the modeled synchrotron emission should match the measured X-ray data of that region (see Eq. 2.12). In order to better understand this disagreement, it is useful to look at the maximum energy of the injection lepton spectrum. Due to the low magnetic field strength, the synchrotron limit becomes irrelevant compared to the gyroradius limit (reviewed in Section 5.1.3) for both scenarios. For the best parameter sets, $E_{e,max}$ is then equal to 429 erg (2.68×10^{14} eV) for *Scenario (a)* (8.5 kpc) and 491 erg (3.07×10^{14} eV) for *Scenario (b)* (13 kpc), respectively. The lepton spectrum is thus comparable to the one used to demonstrate the synchrotron emission in Fig. 2.3 since the cutoff energy is of the same order of magnitude[4]. Therefore the synchrotron emission of the injection spectrum used for the modeling should be roughly resembling the red curve (where $B = 10\,\mu$G) in the figure. As can be easily seen, the keV energy range of the synchrotron emission under such conditions is already strongly affected by the cutoff, and hence Eq. 2.12 is not valid any more, leading to a higher spectral index.

As mentioned, $E_{e,max}$ is given by the gyroradius limit in both scenarios, which is proportionally related to ϵ (see Eq. 5.12). Thus, varying ϵ might significantly influence the spectral shape of our results in the observed energy range. For the scenarios *(a)* and *(b)*, ϵ was fixed to a value of 0.2. As, however, there is no known compelling argument against choosing a higher value in the case of G0.9+0.1, we carried out a third parameter optimization where this parameter was left free in the range $0 < \epsilon < 1$. Having revealed the similarities of the best-fit results for different distance scenarios, we considered it sufficient to perform this new optimization with only one assumed distance. We arbitrarily set $d = 13$ kpc, just as for *Scenario (b)*. The results of the new *Scenario (c)* are presented in the following.

The evolution of the spectral index for that scenario is shown in Fig. 5.10. Compared to the first two scenarios, the spectral index of the first annulus is obviously lower, supporting the assumption that a variation of ϵ indeed has a strong influence on the cutoff of the synchrotron spectrum. In this scenario the shape of the evolution also seems to be rather flat. Just as for Fig. 5.8 and the right panel of Fig. 5.9, the evolution of the surface brightness for *Scenario (c)* is illustrated in Fig. 5.11. The measured values are also well reproduced by the modeled ones of this scenario. Since ϵ was not fixed any more, the parameters are now even more strongly correlated. Where for *Scenarios (a)* and *(b)* it was possible to give explicit values of the parameters with the best-matching results, in the case of *Scenario (c)* there are several quite different parameter sets with similar χ^2 values. The lower and upper values of the parameters for *Scenario (c)* with a χ^2 maximum of 10 % above the lowest obtained value are shown in Table 5.2. However, only certain parameter combinations lead to a good fit result.

[4]The spectral index is also identical

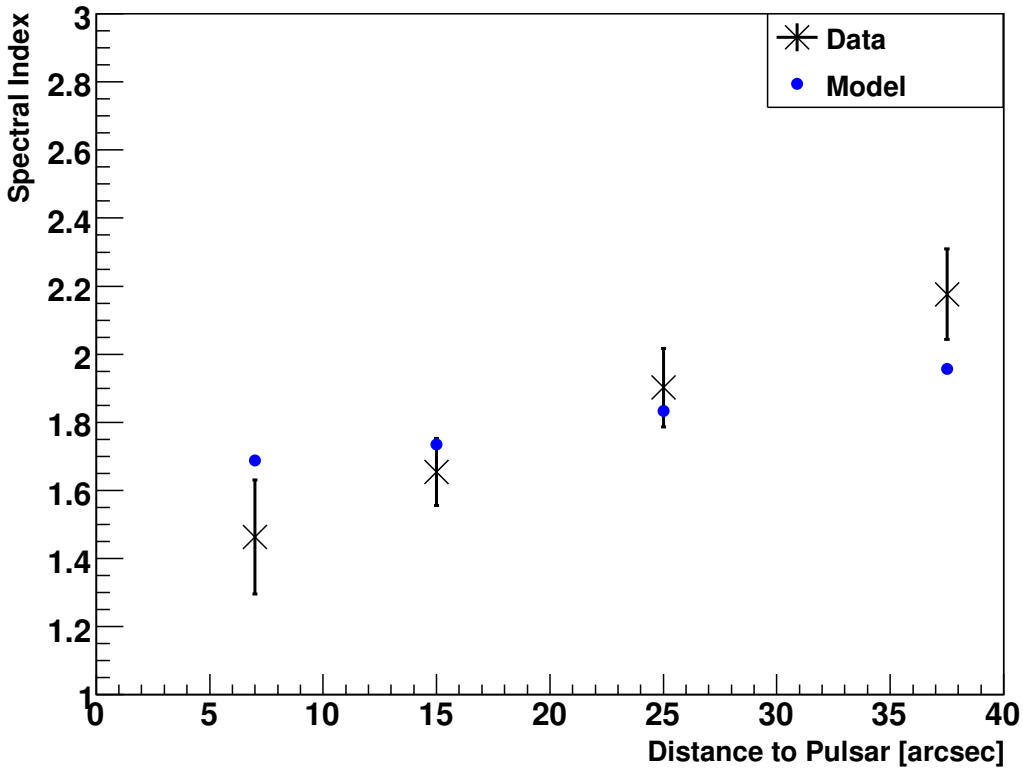

Fig. 5.10.: *Measured and modeled index for Scenario (c). Compared to Fig. 5.7 and the left panel of Fig. 5.9, the shape is obviously different.*

Table 5.2.: *Lower and upper values of the parameters for Scenario (c) with a χ^2 maximum of 10 % above the lowest obtained value. Note that not any arbitrary combination of these parameters leads to a low χ^2 value.*

Parameter	Range
η	$0.38 - 0.55$
ξ	$0.06 - 0.12$
α	$1.22 - 1.28$
φ_S [arcsec]	$2.8 - 4.0$
ϵ	$0.4 - 1.0$
R_S [pc]	$0.18 - 0.25$
B_S [μG]	$4.2 - 5.9$

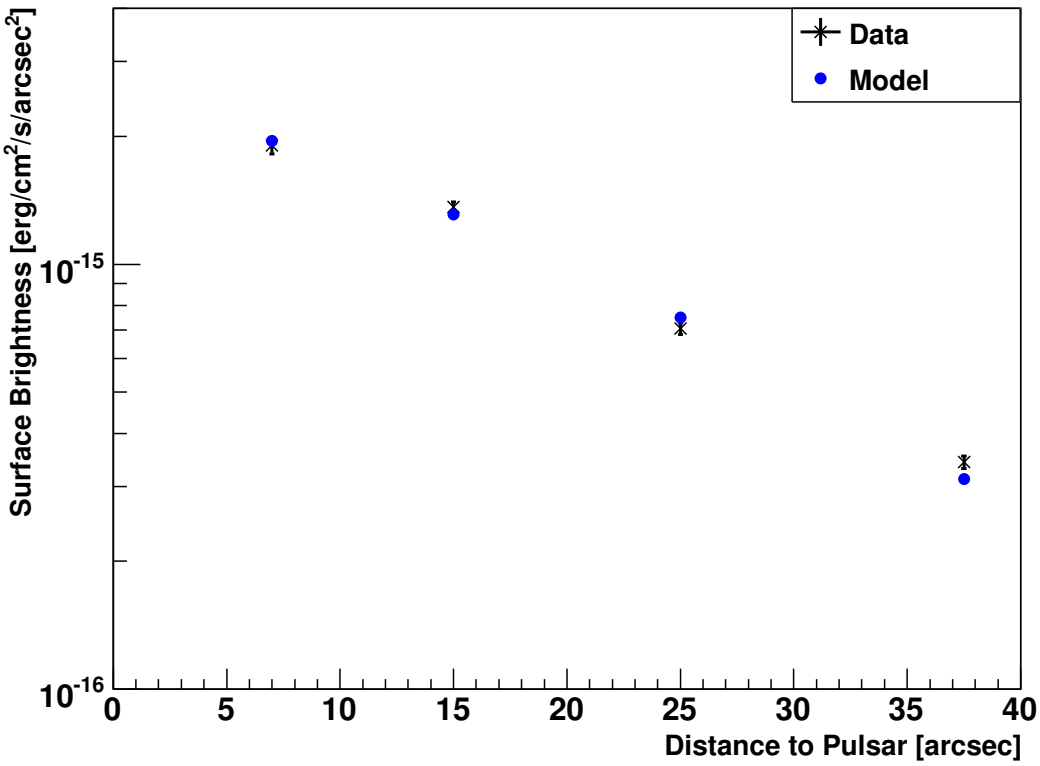

Fig. 5.11.: *Measured and modeled surface brightness for Scenario (c).*

Another interesting result of the modeling to take a closer look at is the radial dependence of the magnetic field strength. It can be calculated via Eq. 5.24. Using this relation, the magnetic field strength is plotted as a function of distance in Fig. 5.12 for the best obtained parameters of all scenarios. Due to the ambiguity of the best-fit parameters of *Scenario (c)*, the magnetic field strength is not well constrained in that situation. Therefore the upper and lower values are shown in the figure. Since the velocity index α is greater than 1 for all scenarios, the magnetic field increases with growing distance to the pulsar, raising the question of the model's validity. However, as we are only focusing on the inner part of the PWN, this feature should not be considered as a show-stopper. With even greater distance, the ideal MHD limit no longer holds, implying that the magnetic field is not frozen into the particle propagation any more. Furthermore it is worth noting that Kennel & Coroniti (1984a) obtained a similar result for the evolution of the magnetic field strength of the Crab nebula.

5.7. Comparing the Modeled TeV γ-ray Emission with the H. E. S. S. Results

The scope of the applied model is not only limited to the X-ray regime. Assuming that the same population of outward propagating leptons that emit synchrotron radiation also scatters photons up into the VHE regime through the IC effect, it is possible to calculate this IC photon flux analogously to the synchrotron emission. The results can afterwards

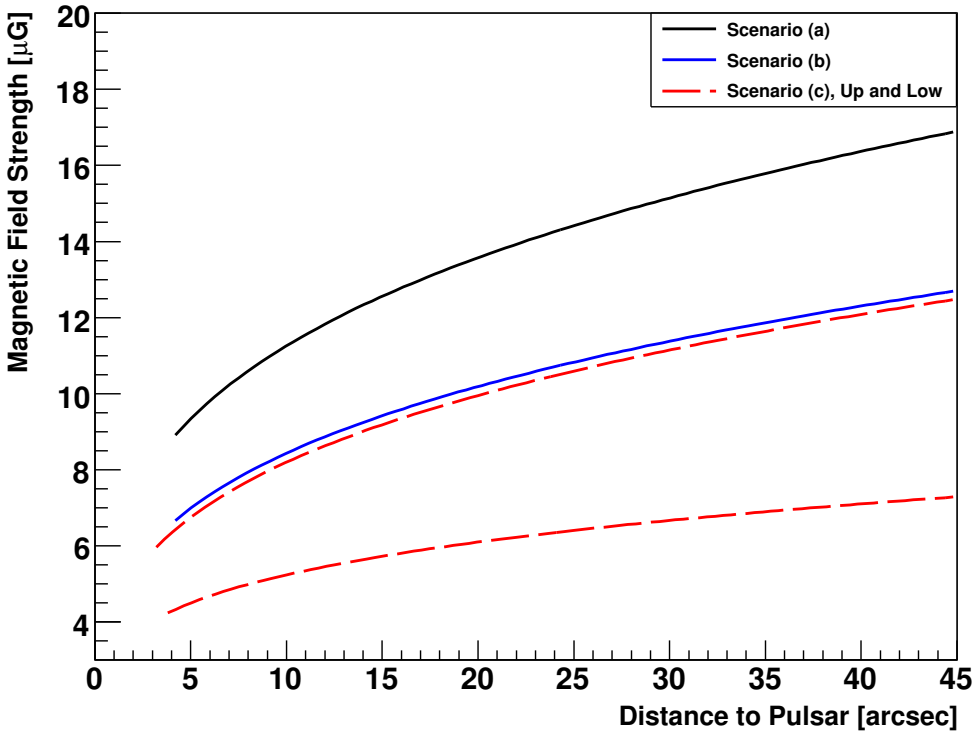

Fig. 5.12.: *Radial dependence of the magnetic field strength for all three scenarios. For scenarios (a) and (b) the best-fit parameters (Table 5.1) were used. The two red curves correspond to the lowest and highest obtained values obtained from the optimization of Scenario (c) (see also Table 5.2).*

be compared with the measured data taken by imaging atmospheric cherenkov telescopes (IACT).

5.7.1. Seed Photon Fields

It was already briefly described in Section 2.1.2 that, in the case of G0.9+0.1, essentially three seed photon fields need to be considered for the IC process: The CMB component, IR photons emitted from local dust and the starlight component. The CMB spectrum is well described by a blackbody distribution with $T = 2.725\,\mathrm{K}$ and an energy density of $4.20 \times 10^{-13}\,\mathrm{erg/cm^3}$ for arbitrary positions. Regarding the IR and starlight fields, however, the situation is far more complicated. Since both are of local origin, their contribution strongly depends on the location of the investigated object. Specifically concerning G0.9+0.1, the positional uncertainty coupled with the source's projected location near the GC permits a great variety of possible field strengths.

As an approximation of the IR and starlight components, we used the interstellar radiation fields (ISRF) of Porter & Strong (2005) developed for the GALPROP code (Strong et al. 2000). Using a cylindrical coordinate system with the GC set as the point of origin and the r-φ-plane equaling the galactic plane, an estimation of the ISRF spectra can be retrieved for arbitrary r and z values.

Table 5.3.: *Photon flux and spectral index of the H.E.S.S. and modeled data of all scenarios. The values of the measured data are taken from Aharonian et al. (2005).*

	Photon Flux$^{(*)}$ ($10^{-12}\,\mathrm{cm}^{-2}\,\mathrm{s}^{-1}$)	Γ
H.E.S.S. Data	5.5 ± 0.8	2.29 ± 0.14
Sc. (a)	0.31	1.66
Sc. (b)	0.38	1.65
Sc. (c)	0.56	1.61

$^{(*)}$ Energy range $0.2 - 10\,\mathrm{TeV}$

5.7.2. Results and the Upscaling Problem

Just as done for the synchrotron emission, the IC radiation was calculated for the best parameter sets (see Table 5.1 for the ones of scenarios *(a)* and *(b)*) of all scenarios. Afterwards the contribution of all shells was summed up. The result is the modeled IC emission up to 45 arcseconds. As already mentioned in Section 2.2, G0.9+0.1 was also detected in VHE γ-rays by H.E.S.S.. This enables a comparison of the modeled IC with the measured data as shown in Table 5.3. Obviously the absolute values as well as the spectral shape strongly deviate. The reasons for this are discussed in the following. In Section 2.2 it was described that G0.9+0.1 is a point source as seen by H.E.S.S.. When assuming a spatial emission distribution of

$$\rho \propto e^{-\frac{\theta^2}{2\sigma^2}}, \tag{5.40}$$

with θ the angular separation from the maximum, the upper limit on the extension is $\sigma < 1.3'$ on a 95 % confidence limit (Aharonian et al. 2005)[5]. The modeling, however, only regards the inner 45 arcseconds of the PWN, neglecting a great part of the emission. Therefore we do not even expect the modeled emission to coincide with the measured one. This problem cannot be solved by extending the model to larger distances since the assumption of a steady-state solution would then no longer hold. A rough estimation of the modeled VHE radiation of the whole PWN can be obtained by scaling up the flux of the modeled part by a certain factor. Woefully the source's extent and spatial distribution in VHE γ-rays is not known. Therefore it is only possible to calculate an upper limit of that factor under the assumption of an emission as given in Eq. 5.40. Using $\sigma = 1.3'$, approximately 15 % of the radiation is contained within 45 arcseconds around the center. Scaling the modeled emission correspondingly, the upper limit on the flux is $2.0 \times 10^{-12}\,\mathrm{cm}^{-2}\,\mathrm{s}^{-1}$ for *Scenario (a)*, $2.5 \times 10^{-12}\,\mathrm{cm}^{-2}\,\mathrm{s}^{-1}$ for *Scenario (b)*, and $3.7 \times 10^{-12}\,\mathrm{cm}^{-2}\,\mathrm{s}^{-1}$ for *Scenario (c)*, respectively. Although the values still lie below the measured one, they are already of the same order of magnitude. As can also be seen by looking at Table 5.3, the modeled spectral index lies well below the measured one in all cases. This deviation can also be explained by the same effect. Similar to the synchrotron radiation, the spectral index of the IC photon spectra is also expected to increase with larger distance to the pulsar. Fig. 5.13 illustrates the evolution of the spectral index for the

[5] It was also mentioned that the authors alternatively suggest an upper limit for the emission from a thin shell. Since such a distribution is clearly not expected for G0.9+0.1, it will not be taken into account in the following.

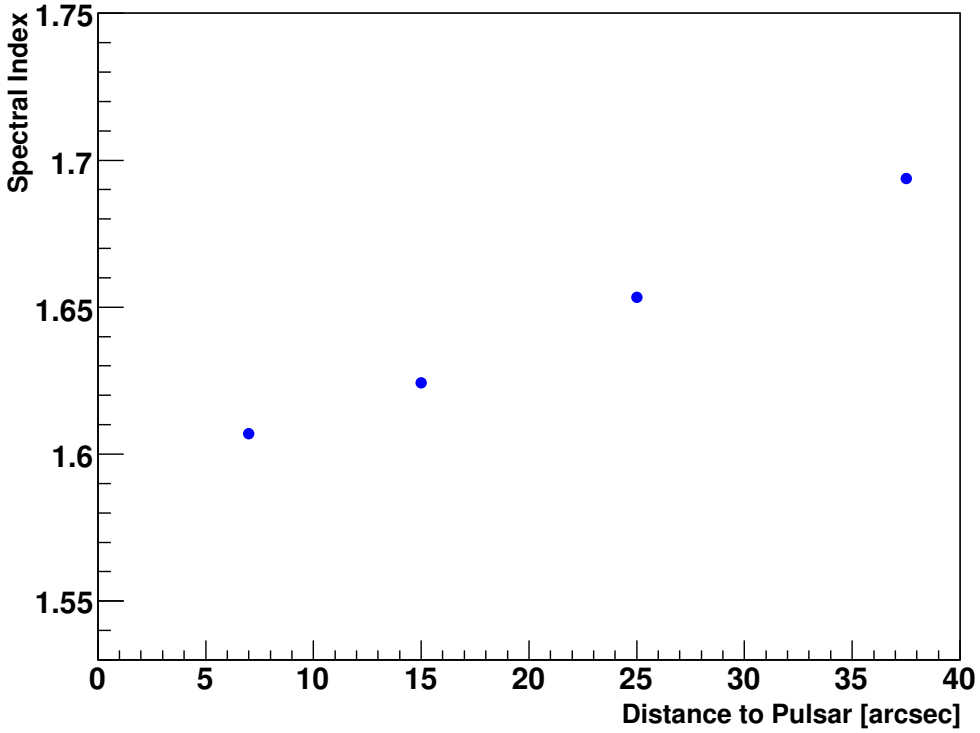

Fig. 5.13.: *Evolution of the spectral index of the IC emission with increasing distance to the pulsar for Scenario (b).*

modeled area in the case of *Scenario (b)*. Therefore, a lower spectral index of the modeled IC emission compared to the measured VHE data is indeed expected. However, since our model is limited to the most inner part of the PWN, we are not able to quantitatively estimate the influence of this effect for larger distances.

Independent of the previous discussion, it has to be recalled that the estimation of the photon fields may be substantially in error, which might heavily influence the IC results.

The last results to be discussed in this work are the spectral energy distributions (SED) of the three scenarios. The one for *Scenario (c)* is shown in Fig. 5.14. It comprises the measured *XMM-Newton* data of the whole modeled area as well as the VHE γ-ray results of the H. E. S. S. collaboration published in Aharonian et al. (2005). The red and blue curves correspond to the modeled synchrotron and IC emission. The contributions of the individual photon fields to the IC emission are also shown. The synchrotron emission obviously reproduces the measured X-ray data well. In contrast to that, the IC emission strongly deviates from the VHE data concerning the spectral shape as well as the absolute values. Possible reasons for this have already been discussed in this Section. Especially it has to be noted that the measured γ-rays are expected to be emitted from a far greater area than the modeled ones, and therefore a comparison between both is hardly possible. Similar to Fig 5.14, the SEDs for the scenarios *(a)* and *(b)* are illustrated in Fig. 5.15. As already discussed in Section 5.6, the results of these scenarios are very similar, leading to a hardly distinguishable spectral shape of the synchrotron emission. The modeled IC emission however slightly deviates, originating in the different assumed seed photon fields of both scenarios. Compared to *Scenario (c)*, the IC flux is obviously lower in both cases.

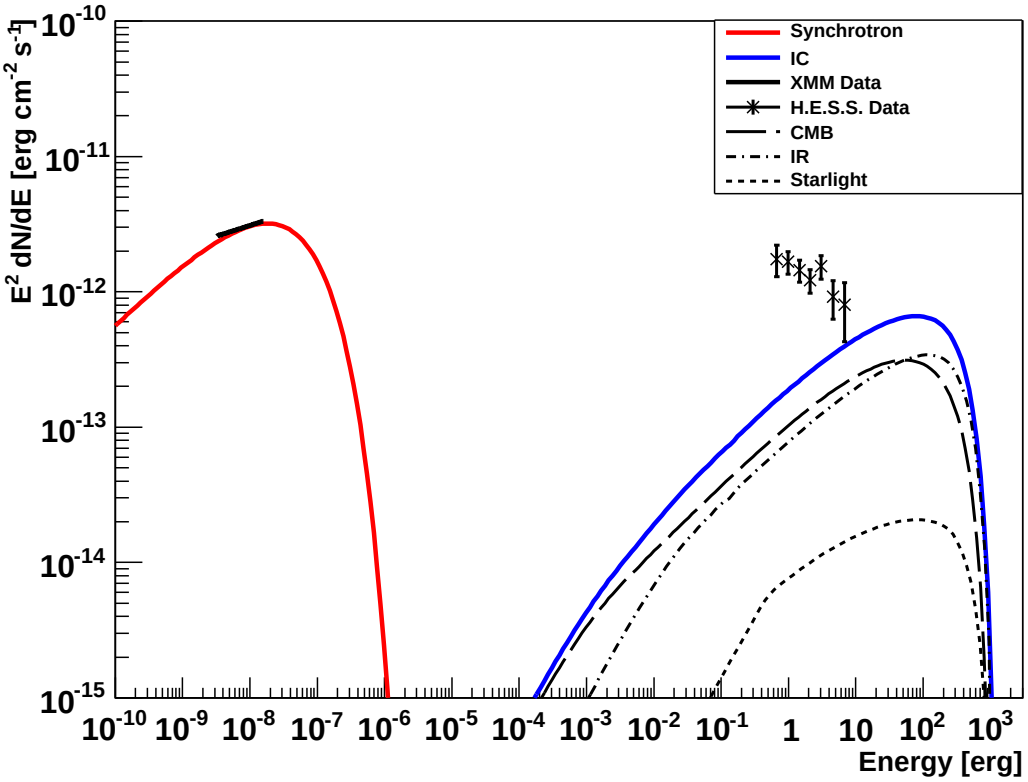

Fig. 5.14.: *Spectral energy distribution of G0.9+0.1 showing the synchrotron and IC emission of the modeled area as obtained for Scenario (c). Also included are the measured XMM-Newton data of the modeled area as well as the H. E. S. S. data of the whole PWN (Aharonian et al. 2005).*

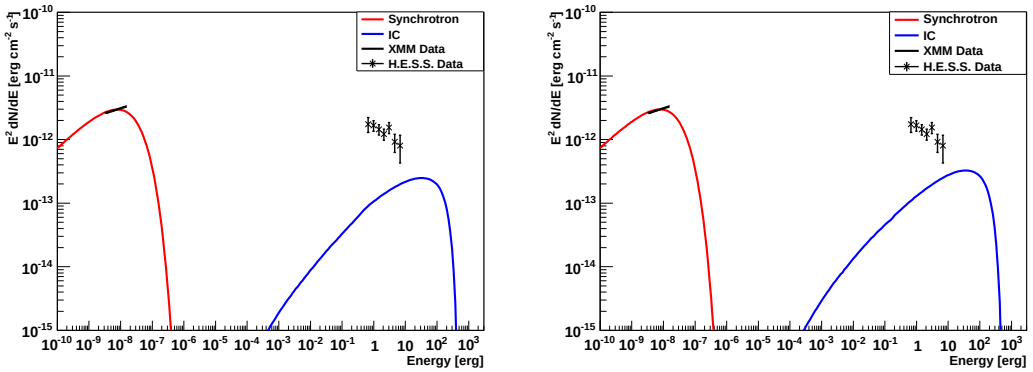

Fig. 5.15.: *Left: Spectral energy distribution of Scenario (a), analogously illustrated as in Fig. 5.14. Right: Spectral energy distribution of Scenario (b).*

In this figure it is also easy to see that the synchrotron emission is already strongly affected by the cutoff in the energy range of *XMM-Newton* for these scenarios, as already discussed in Section 5.6.

6. Conclusion and Outlook

In this work, the non-thermal emission of the PWN in the SNR G0.9+0.1 was extensively analyzed. Following a brief introduction about PWNe and the relevant radiation processes, the current knowledge about G0.9+0.1 and its pulsar PSR J1747−2809 was discussed. Due to the source's projected location near the galactic center, the absorption in the X-ray domain is very strong. With its high effective area, the imaging X-ray telescope *XMM-Newton* is well suited for the spectral analysis of an extended, strongly absorbed source like G0.9+0.1. Two data sets of G0.9+0.1 from *XMM-Newton* were analyzed, particularly emphasizing on a correct background treatment and the grouping of the spectra. The spectral properties of photons from annulus-shaped regions, centered on the putative position of PSR J1747−2809, were investigated. Fitting an absorbed power law to each of the spectra, it turned out that the spectral index increases with larger distance to the pulsar, reflecting a softening of the emission. Similarly, the surface brightness of the chosen annuli decreases with larger distance to PSR J1747−2809. A model was applied in order to reproduce the measured X-ray emission from G0.9+0.1. Given certain parameters containing information about the pulsar and its leptonic outflow, the synchrotron emission of these leptons can be calculated and compared with the analyzed *XMM-Newton* data. The model parameters were optimized separately for three scenarios, assuming different distances to G0.9+0.1 as well as different limits on the particle acceleration inside the PWN. It shows that all scenarios are able to explain the measured data well, however the evolution of the modeled spectral index is rather flat for all scenarios. Using the best-fit parameters of the scenarios, the IC emission of the leptons was calculated for the modeled part of G0.9+0.1 and compared with the results in the VHE range measured with H. E. S. S.. For all scenarios, the obtained photon flux is an order of magnitude below the published one. The spectral index of the IC emission is also very low compared to the value fitted to the measured data. However, both effects were expected to a certain degree since the modeled area only corresponds to the inner part of the PWN. Since the source's extent in VHE γ-rays is not known, an appropriate comparison between modeled and measured data is hardly possible.

G0.9+0.1 is the second PWN to which this model was applied. It is especially successful in reproducing the emission and spatial evolution in X-rays. Calculating the IC emission and comparing it with measured data in VHE γ-rays is a good method to dispassionately check the leptonic interpretation of PWNe. Therefore the model is going to be adopted to G21.5−0.9 and other suitable PWNe in the near future. Another goal is to generalize its scope further, for example by implementing a time-dependence as well as a toroidal instead of a radial magnetic field.

A. *XMM-Newton* Spectra of the Four Annuli

In the following, the *XMM-Newton* spectra extracted from all four annuli are shown. For a detailed explanation, the reader is referred to Chapter 4.

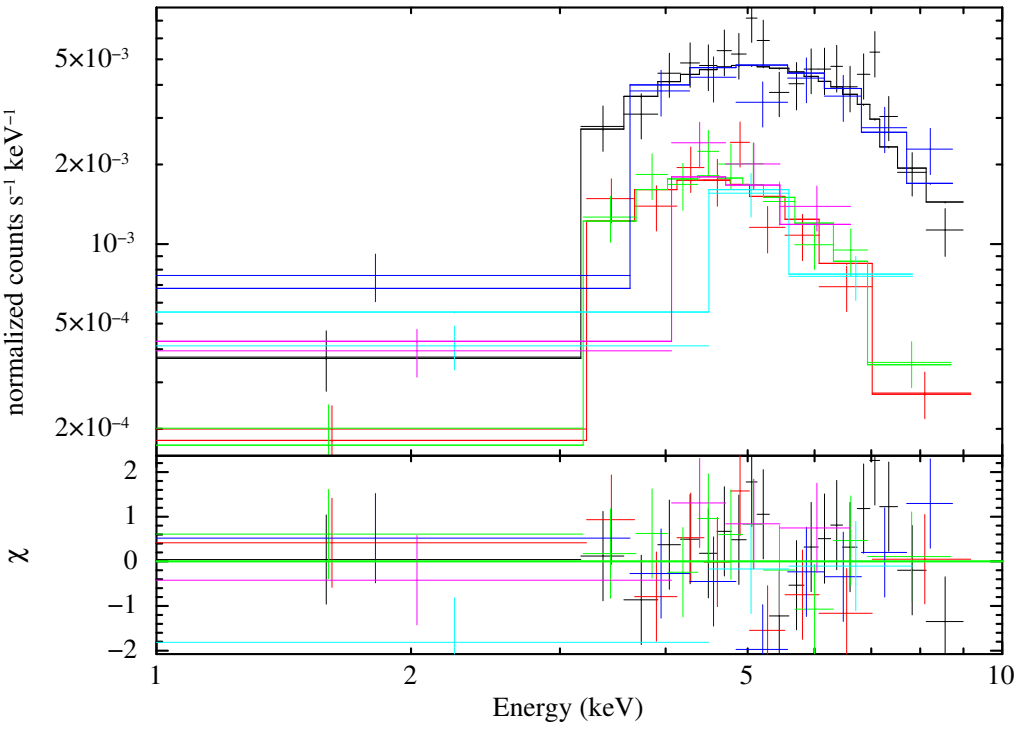

Fig. A.1.: *Energy spectrum extracted from the first annulus.*

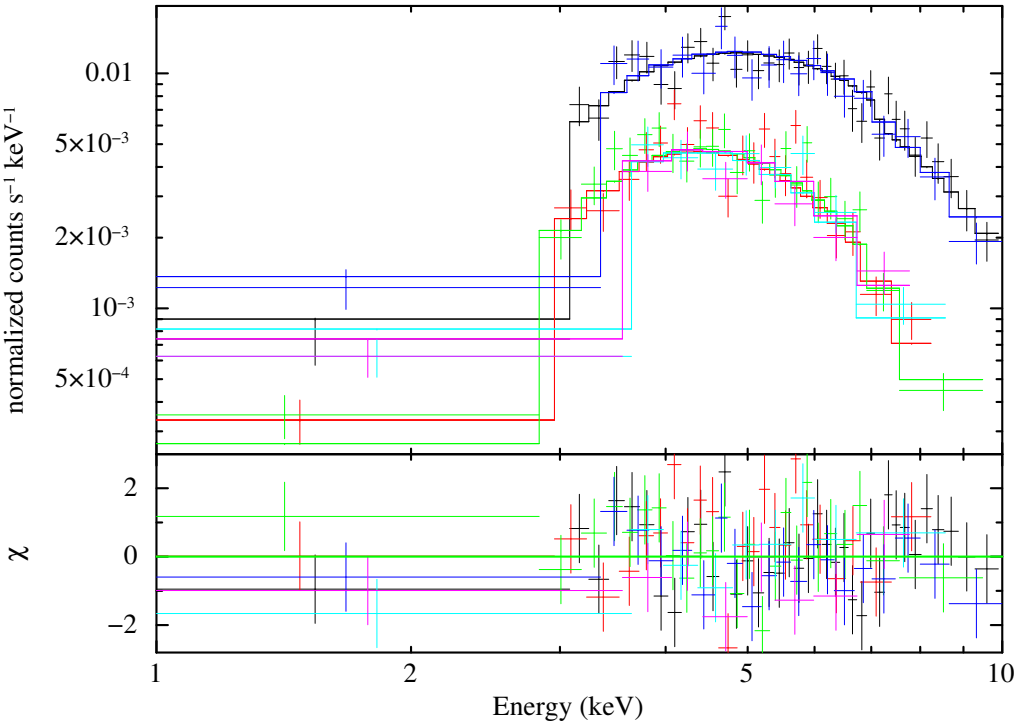

Fig. A.2.: *Energy spectrum extracted from the second annulus.*

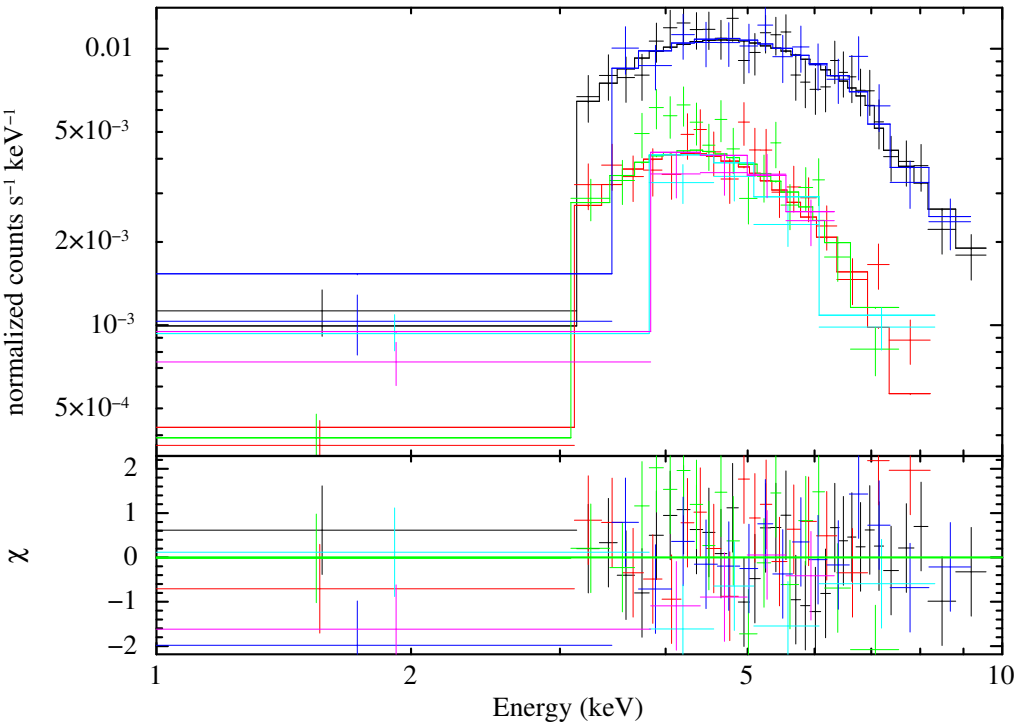

Fig. A.3.: *Energy spectrum extracted from the third annulus.*

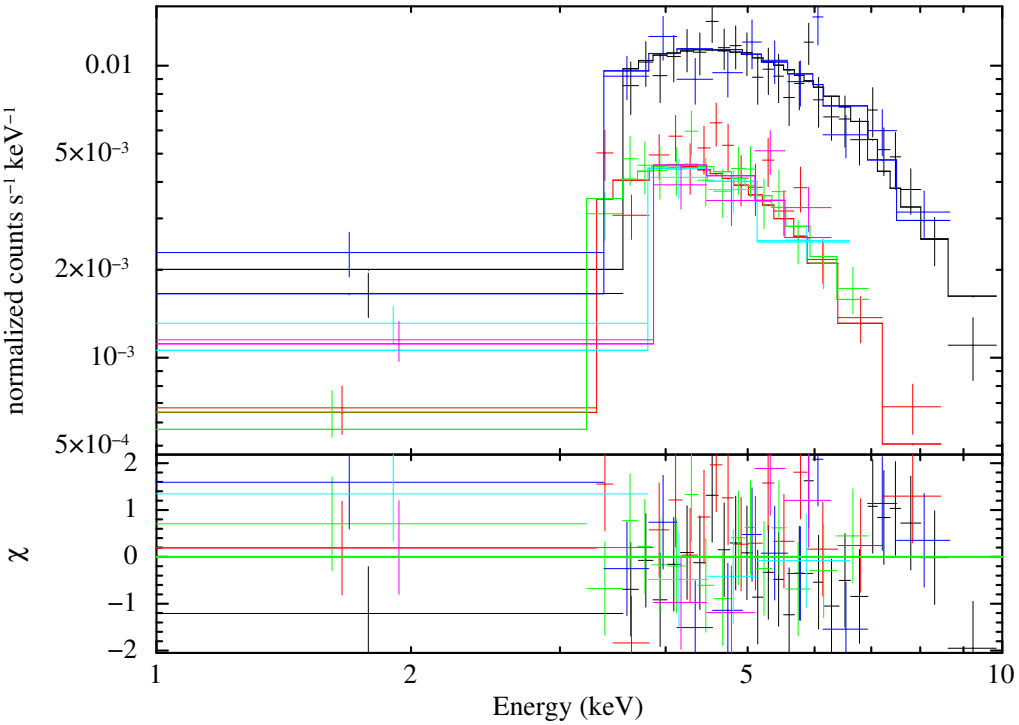

Fig. A.4.: *Energy spectrum extracted from the fourth annulus.*

List of Figures

List of Tables

Bibliography

Aharonian, F., Akhperjanian, A. G., Aye, K., et al. 2005, A&A, 432, L25

Aharonian, F. A. & Bogovalov, S. V. 2003, New Astronomy, 8, 85

Arnaud, K. A. 1996, in Astronomical Society of the Pacific Conference Series, Vol. 101, Astronomical Data Analysis Software and Systems V, ed. G. H. Jacoby & J. Barnes, 17

Arnaud, M., Neumann, D. M., Aghanim, N., et al. 2001, A&A, 365, L80

Blackburn, J. K. 1995, in Astronomical Society of the Pacific Conference Series, Vol. 77, Astronomical Data Analysis Software and Systems IV, ed. R. A. Shaw, H. E. Payne, & J. J. E. Hayes, 367

Blumenthal, G. R. & Gould, R. J. 1970, Reviews of Modern Physics, 42, 237

Camilo, F., Ransom, S. M., Gaensler, B. M., & Lorimer, D. R. 2009, ApJ, 700, L34

Camilo, F., Ransom, S. M., Gaensler, B. M., et al. 2006, ApJ, 637, 456

Collins, II, G. W., Claspy, W. P., & Martin, J. C. 1999, PASP, 111, 871

Cordes, J. M. & Lazio, T. J. W. 2002, ArXiv Astrophysics e-prints

de Jager, O. C. & Djannati-Ataï, A. 2008, ArXiv e-prints

de Jager, O. C. & Harding, A. K. 1992, ApJ, 396, 161

de Jager, O. C., Harding, A. K., Michelson, P. F., et al. 1996, ApJ, 457, 253

den Herder, J. W., Brinkman, A. C., Kahn, S. M., et al. 2001, A&A, 365, L7

Dubner, G., Giacani, E., & Decourchelle, A. 2008, A&A, 487, 1033

Gaensler, B. M., Pivovaroff, M. J., & Garmire, G. P. 2001, ApJ, 556, L107

Gaensler, B. M. & Slane, P. O. 2006, ARA&A, 44, 17

Harding, A. K. & Gaisser, T. K. 1990, ApJ, 358, 561

Helfand, D. J. & Becker, R. H. 1987, ApJ, 314, 203

Jansen, F., Lumb, D., Altieri, B., et al. 2001, A&A, 365, L1

Joye, W. A. & Mandel, E. 2003, in Astronomical Society of the Pacific Conference Series, Vol. 295, Astronomical Data Analysis Software and Systems XII, ed. H. E. Payne, R. I. Jedrzejewski, & R. N. Hook, 489

Kennel, C. F. & Coroniti, F. V. 1984a, ApJ, 283, 694

Kennel, C. F. & Coroniti, F. V. 1984b, ApJ, 283, 710

Kesteven, M. J. L. 1968, Australian Journal of Physics, 21, 369

Klein, O. & Nishina, T. 1929, Zeitschrift für Physik, 52, 853

Li, T. & Ma, Y. 1983, ApJ, 272, 317

Majerowicz, S., Neumann, D. M., & Reiprich, T. H. 2002, A&A, 394, 77

Mason, K. O., Breeveld, A., Much, R., et al. 2001, A&A, 365, L36

Matheson, H. & Safi-Harb, S. 2005, Advances in Space Research, 35, 1099

Mereghetti, S., Sidoli, L., & Israel, G. L. 1998, A&A, 331, L77

Porquet, D., Decourchelle, A., & Warwick, R. S. 2003, A&A, 401, 197

Porter, T. A. & Strong, A. W. 2005, in International Cosmic Ray Conference, Vol. 4, International Cosmic Ray Conference, 77

Reynolds, S. P. & Chevalier, R. A. 1984, ApJ, 278, 630

Schöck, F. M. 2010, Dissertation, Friedrich-Alexander-Universität, Erlangen, Germany

Schöck, F. M., Büsching, I., de Jager, O. C., Eger, P., & Vorster, M. J. 2010, A&A, 515, A109

Sefako, R. R. & de Jager, O. C. 2003, ApJ, 593, 1013

Short, A. D., Keay, A., & Turner, M. J. 1998, in Presented at the Society of Photo-Optical Instrumentation Engineers (SPIE) Conference, Vol. 3445, Society of Photo-Optical Instrumentation Engineers (SPIE) Conference Series, ed. O. H. Siegmund & M. A. Gummin, 13–27

Sidoli, L., Mereghetti, S., Israel, G. L., & Bocchino, F. 2000, A&A, 361, 719

Slane, P. 2010, ArXiv e-prints

Strong, A. W., Moskalenko, I. V., & Reimer, O. 2000, ApJ, 537, 763

Strüder, L., Briel, U., Dennerl, K., et al. 2001, A&A, 365, L18

Turner, M. J. L., Abbey, A., Arnaud, M., et al. 2001, A&A, 365, L27

Wilms, J., Allen, A., & McCray, R. 2000, ApJ, 542, 914

Wolter, H. 1952, Annalen der Physik, 445, 94

Danksagung

Im Folgenden möchte ich mich bei einigen Personen bedanken, die durch ihre Unterstützung maßgeblich zum Gelingen dieser Diplomarbeit beigetragen haben:

- Der kompletten Erlanger H. E. S. S.-Gruppe, in der nicht nur das Teetrinken Spaß macht, sondern auch die Arbeitsatmosphäre sehr angenehm ist.
- Prof. Dr. Christian Stegmann, der es immer wieder aufs Neue schafft, einen für die Physik zu motivieren und sich trotz seiner vielfältigen Verpflichtungen immer Zeit nimmt Fragen zu beantworten.
- Peter Eger und Fabian Schöck, die mich beide nicht nur hervorragend betreut haben, sondern mit denen es auch sonst nie langweilig wurde.
- Dr. Kathrin Valerius, durch deren Korrekturen an der Diplomarbeit meine Englischkenntnisse ordentlich aufpoliert wurden.
- Michael Mayer, für sein Verständnis, dass man sich auch mit *so niederergetischem Zeug* wie der Röntgenanalyse befassen kann. Sads fraindlich!
- Anneli Schulz, Kornelia Stycz, Arnim Balzer und allen anderen für entspannte Kaffee- bzw. Teerunden.
- Meinen Eltern und Brüdern für die nötige Unterstützung, ohne die ein Studium nicht möglich gewesen wäre.

Erklärung

Ich bestätige hiermit, dass ich die vorliegende Diplomarbeit selbständig verfasst und keine anderen als die angegebenen Quellen und Hilfsmittel verwendet habe.

Erlangen, den 15. Oktober 2010